HeriTACE

ETICS solution for plastered masonry walls

Deliverable D2.3

Version N° 1.0

DOI: 10.5281/zenodo.21024740

Authors: Paul Klõšeiko (TALTECH), Kristina Vilba (TALTECH), Martin Talvik (TALTECH), Rene Vinkler (SAKRET)

Funded by the European Union

Disclaimer

Project information

Grant Agreement	n°101138672
Project Title	Future-proofing Heritage Townhouses by Optimising Comfort and Energy in Time and Space
Project Acronym	HeriTACE
Project Coordinator	Arnold Janssens, Ghent University
Project Duration	1 January 2024 - 31 December 2027 (48 months)

Deliverable information

Related Work Package	WP2: Energy efficient and durable building envelope solutions for heritage buildings
Related Task(s)	T2.3 Durable exterior insulation solutions which age faithfully to the original facades
Lead Organisation	TALTECH
Contributing Partner(s)	TALTECH, SAKRET
Due Date	M30
Submission Date	29/06/2026
Dissemination level	SEN

History

Date	Version	Submitted by	Reviewed by	Comments
30/06/2026	1.0	Paul Klõšeiko (TALTECH)	Nathan Van Den Bossche	Submitted

Table of Contents

List of Figures

List of Tables

Glossary

Acronym/abbreviation/term	**Description**
archetype	Here: a pattern or a type of building with common traits/configurations that represents a subset of buildings in the targeted neighbourhoods
CFD	Computational Fluid Dynamics
EPS	Expanded polystyrene (insulation)
ETICS	External Thermal Insulation Composite System
EU	European Union
FTC	Freeze-thaw cycle
HeriTACE	Future-proofing HERItage Buildings by Optimising Comfort and Energy in Time and spACE
HFM	Heat flow meter
KAM-R	Lime-cement plaster SAKRET KAM-R
LC	Lime-cement (plaster)
MI	Mould index (according to the Finnish Mould Model)
MW	Mineral wool (insulation)
NHL	Natural hydraulic lime
PF	Phenolic foam (insulation)
RH	Relative humidity
TPS	Transient plane source
UPV	Ultrasonic pulse velocity
WDR	Wind driven rain
WFB	Wood fiberboard (insulation)
WP	Work package

Executive Summary

Overview

As part of WP2, Task T2.3 focuses on developing and evaluating exterior insulation solutions compatible with historical plastered masonry facades. The task aims to balance the preservation of cultural heritage with the project's overarching goal of reducing building energy demand by 60% while also improving the poor hygrothermal performance of the masonry wall.

A thorough multi-scale investigation evaluated the hygrothermal properties and durability of 2 exterior thermal insulation composite systems (ETICS): one based on thick layers of NHL-based plasters (Sakret NHL-1 & NHL-2), while the second was based on thin lime-cement (Sakret KAM-R) plaster. Four insulation materials (mineral wool, EPS, wood fiberboard, phenolic foam) were evaluated in combination with both plaster systems. The study utilized a combination of material-level testing, climate chamber experiments, outdoor test wall monitoring, and hygrothermal modeling to assess moisture management and frost resistance.

Outcomes

Material level measurements provided the hygrothermal properties required for modelling. These also showed that the onset of frost damage across all tested plasters occurred between 70–100% saturation, which now serves as a performance criterion for modelling. A clear correlation was identified between frost damage and a 3–5x increase in water uptake coefficients.

Measurements from the climate chamber study and outdoor test wall provide valuable reference data on the responses of various ETICS combinations to both extreme and realistic climatic conditions. The outdoor test wall also served as a successful platform for validating construction technologies.

Modelling indicates that the hygrothermal performance is heavily dependent on wind-driven rain (WDR) loads. In high-WDR environments, the application of hydrophobing agents is likely necessary to protect NHL plaster systems, though these agents show limited efficacy under prolonged water contact.

Conclusions

The outdoor test wall drew positive engagement from municipal authorities and homeowners, underscoring real-world demand for compatible insulation solutions that deliver both energy performance and respect heritage value – reinforcing the need for continued development and uptake of these systems.

While current hygrothermal models are conservative (potentially overestimating moisture absorption by 1.5–2x), they provide a baseline for risk assessment. While TRL 5 was reached here, future research could focus on refining liquid transfer functions for more accurate modelling, accounting for paint/hydrophobation effects, and scaling the test wall to larger-scale building applications with complex joints.

1. Introduction

The ambitions of the European Union (EU) are substantial: to achieve climate neutrality by 2050. The European Green Deal and the New European Bauhaus aim to achieve a sustainable and inclusive society through transdisciplinary collaboration and innovation. However, one of the most significant challenges in this transition will be the renovation wave of our housing stock, which accounts for 27% of the final energy use of the EU (Eurostat, 2022). Historic cities in Europe present an additional challenge. It is evident that the historically valuable buildings in these cities must be preserved while respecting and considering the inherent heritage and societal values. However, it is unclear how we can balance the aspirations on heritage conservation on individual units with the overarching ambition for climate neutrality at the building stock level. More specifically, there is a need for a framework to assess these different aspects at building or neighbourhood level and offer insights and solutions to address this challenge.

The HeriTACE project investigates how we can future proof our heritage buildings in a manner that bridges the gap between heritage restrictions and environmental ambitions. The project focuses specifically on small to medium-sized heritage townhouses pre-dating 1945. Achieving the ambitious goal of climate-neutrality requires a transdisciplinary team to consider all aspects of renovation: heritage value, energy use, user comfort, functionality, cost-effectiveness, and waste management. Heritage restrictions often preclude generic solutions, necessitating innovative approaches to insulation, heating, ventilation, and heat/cold generation.

1.1 Problem statement

Exterior walls of the Stalinist brick apartment building archetype have low hygrothermal performance: the measured thermal transmittances of the 2 case study buildings of this archetype were 1.1 and 1.5 W/(m²·K) for Sikupilli and Kristiina buildings respectively (see deliverable D2.1). This causes several issues:

- Considerable **thermal losses and high heating costs** during the heating season. For example, the pre-renovation heating energy need of archetypical Stalinist brick apartment building was about 40% higher than that of the wooden apartment building archetype of similar age (see deliverable D3.3).
- Low interior surface temperature of the walls negatively affects **thermal comfort** (also reported as a complaint during the interviews with the inhabitants, see deliverable D5.3).
- **Elevated surface humidity** levels on the wall, especially at joints (e.g. corners), which can cause **mould growth**. In one of the four studied apartments of this archetype, the mould growth was a recurring issue (see Figure 3 and deliverable D2.1).

Figure 1: Kristiina and Sikupilli case study buildings are examples of different sizes of the Stalinist brick apartment building archetype (photos: Paul Klõšeiko).

Figure 2: Examples of facade finish decor variations on the archetypical Stalinist brick apartment buildings (photos from left: Google StreetView, Paul Klõšeiko, Google StreetView, Paul Klõšeiko).

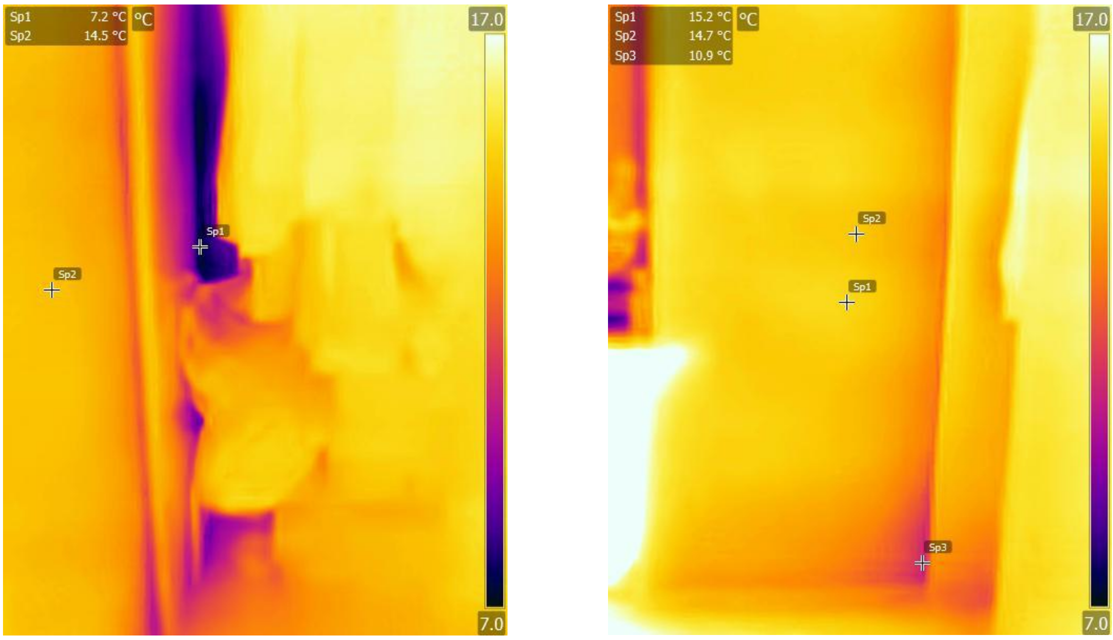

Figure 3: Exterior walls of Stalinist brick apartment buildings (and other buildings with similar mass masonry walls) have poor hygrothermal performance. Here a problematic corner detail of a building in HeriTACE project exhibits recurring mould growth. Sp1 of left thermogram shows surface temperature of the corner that also happens to be behind a cupboard resulting in a very low temperature factor of f_{Rsi} = 0.34. (See deliverable D2.1)

To overcome these issues, **interior insulation** is often seen as a solution as the exterior will stay intact initially. However, interior insulation has considerable shortcomings: thermal resistance achieved using interior insulation is usually ca 2-4 times lower than with exterior insulation, the cost can be significantly higher, installation causes severe disturbance of the inhabitants, reduction of thermal mass on the interior side of the wall may increase overheating risk, thermal bridges remain and can become more critical than before, the risk of frost damage in historic wall increases, etc (Klõšeiko & Kalamees, 2022).

Commonly used **exterior thermal insulation composite systems** (ETICS) are usually considered incompatible with the Stalinist brick apartment building archetype and heritage buildings with plastered facades from the heritage point of view. The main issues being:

- **Too clinical and large grained finishing layer:** due to the insulation boards being produced to tight tolerances, the surface of the finishing layer can seem much more flat and clinical compared to the one on the original facades where thicker plaster layers are applied on the masonry. The commonly used ETICS finishing plasters also have too large grain which is uncharacteristic to the targeted buildings (Figure 4).
- **Insulation board pattern is visible on the finishing layer:** due to thin plaster layer and thermal expansion, the insulation boards can be visible (especially in shallow light angles) – see Figure 5.
- **Aging patterns:** Reduced heat flux through the insulated wall lowers the surface temperature of the facade plaster and lowers the drying potential. Prolonged periods of high humidity result in suitable conditions for biological growth (e.g. mould, algae). Large-grain nature of the modern finishing plasters partly contributes to this – horizontal surfaces support both accumulation of dust as well as moisture while restricting water runoff and self-cleaning. As the insulation fasteners are thermal bridges, the plaster on top of them dries quicker and does not soil as quickly as on the rest of the facade leaving clean spots on the surface.
- **Replication of facade decor:** as the archetypical buildings incorporate a varying degree of characteristic cornices, framings around the windows, etc decor that should be replicated on the new exterior surface. The proper design (in terms of architectural and technical detailing) and implementation is often difficult and requires careful consideration of insulation thicknesses and joints with other envelope components.
- **Low durability and fault intolerance:** the ETICS facades are economical to build and widespread, but unfortunately also suffer from early onset of damage and/or aesthetic issues (Liisma et al., 2016; Olak, Kalamees, et al., 2026). Further problems arise when moisture exists behind the plaster layer – either through water leakages, moisture added during the insulation works and/or the moisture already present in the masonry before the insulation. As the plaster layer is rather vapour tight, it is common for the moisture to accumulate in the plaster and cause frost damage (Figure 6). These effects become more pronounced when most of the façade surface is insulated with EPS, making MW fire breaks mandatory. The non-uniform insulation concentrates moisture loads in the narrow zone of the MW fire breaks, resulting in horizontal linear deterioration, as shown in Figure 7 and discussed in detail in (Olak, Talvik, et al., 2026; Talvik et al., 2023).

Figure 4: Finishing plaster with uncharacteristically large grain size can ruin the final result of the exterior insulation works (photos: Paul Klõšeiko).

Figure 5: Different types of uniformity of the exterior plaster: uninsulated building where the unevenness of masonry and plastering works result in characteristic look (left) and insulated facade, where the pattern of the insulation boards can be distinguished (right). Photos: Paul Klõšeiko.

Figure 6: Examples of damage in ETICS facades: loss of adhesion between finishing and reinforcement layers (left) and extensive frost damage (right). Photos: Paul Klõšeiko.

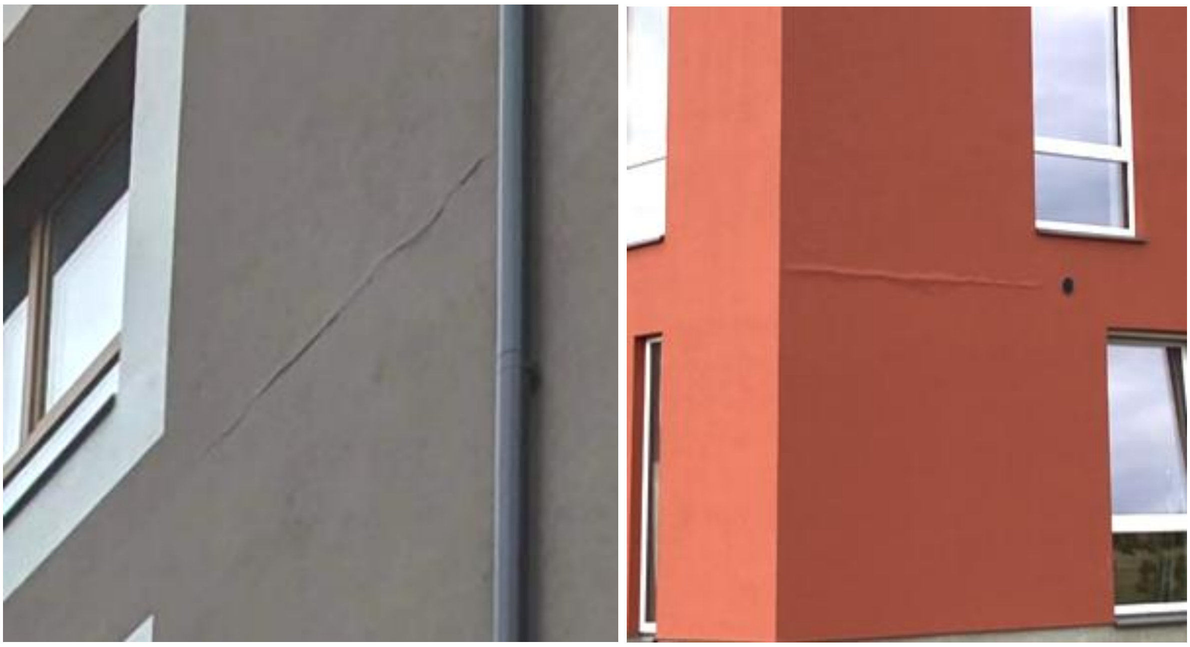

Figure 7: Examples of damage to ETICS facades: cracking along the lower boundary between the EPS main insulation and the mineral wool fire barriers. Photos: Martin Talvik, Targo Kalamees

1.2 Proposed ETICS solutions

As a possible option to overcome at least some of the limitations of the currently available thin-plaster ETICS systems available in Estonia that were described in previous section, SAKRET has developed 2 ETICS solutions to be analysed and assessed in Task 2.3 of this project.

By utilizing thicker plaster layers it is possible to conceal unattractive insulation board patterns and to add a "human touch" to avoid the undesirable "clinical" aesthetic. The smooth surface of the proposed plasters offers greater compatibility with historic finishes compared to the coarse grain of conventional thin-plaster systems. Beyond aesthetics, the higher vapor permeability of these plasters possibly enhances moisture management within the ETICS, also facilitating drying and mitigating moisture accumulation if rain ingress occurs. Solutions for more durable replication of facade decor are proposed.

Table 1: The proposed ETICS systems studied in this task.

<table>
<tr><th>Thick plaster system
(total plaster thickness: 25-30 mm)</th><th>Thin plaster system
(total plaster thickness: ca 10 mm)</th></tr>
<tr><td>Main plaster: natural hydraulic lime plasters SAKRET NHL-1 & NHL-2</td><td>Main plaster: lime-cement plaster SAKRET KAM-R</td></tr>
<tr><td>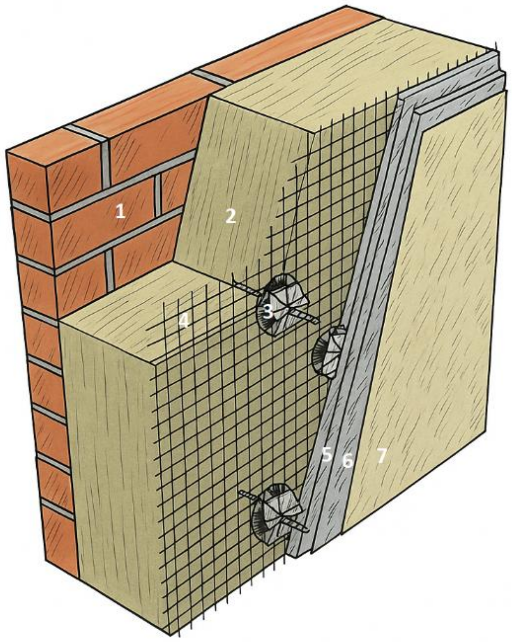
</td><td>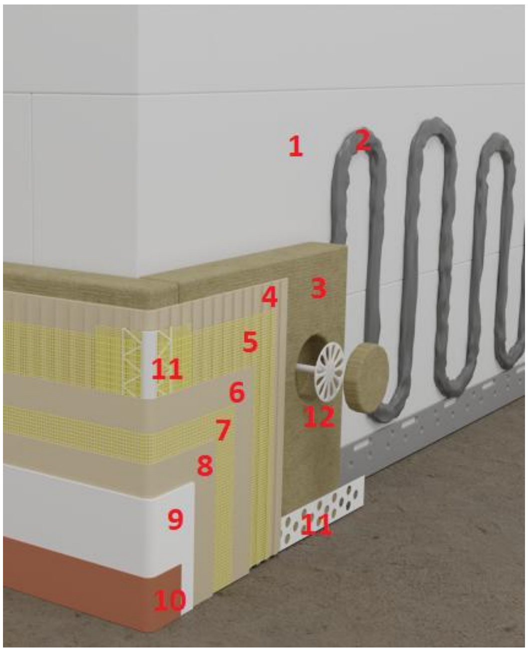
</td></tr>
<tr><td>1. Substrate
(Glued attachment solution: primer + Sakret KAM-R glue mortar)
2. Insulation: EPS, MW, PF, WFB
3. Facade dowels: KDS
4. Steel mesh (12x12...20x20 mm, stainless steel or hot dip galvanized)
5. Base coat: NHL-2 (with KAM-R bonding layer for EPS/PF)
6. Levelling/finish coat: SAKRET NHL-1
7. Paint: SAKRET KFF lime paint (2–3 coats)</td><td>1. Substrate (priming required if glued with SAKRET KAM-R)
2. Adhesive: SAKRET KAM-R
3. Insulation: EPS, MW, PF, WFB
4. Base reinforcement layer: SAKRET KAM-R
5. 1st fibreglass mesh layer (160 g/m²)
6. Intermediate reinforcement layer: SAKRET KAM-R
7. 2nd fibreglass mesh layer (160 g/m²)
8. Levelling layer: SAKRET KAM-R
9. Finish layer: SAKRET KAM-R
10. Paint: SAKRET KS EXTERIOR (2 coats)
11. PVC system profiles
12. Facade dowels with insulation caps</td></tr>
</table>

Thick-plaster system is built using two or, in some cases, three plasters developed specifically for the project: NHL-2 and NHL-1. These consist of hydraulic lime NHL 3.5, small amounts of white Portland cement (for strength and setting control), and organic/inorganic additives. NHL-2 contains sand with grain size up to 2 mm, while NHL-1 uses sand up to 1 mm. NHL-2 is used as bonding and base coat; NHL-1 as levelling and finish coat. Depending on the desired visual finish, NHL-2 can also be used as a topcoat.

For EPS and phenolic foam insulation, a KAM-R adhesive layer was used before applying NHL-2 and NHL-1. For mineral wool and wood-fibre boards no adhesive layer was necessary. Reinforcement of the test wall in this study was done with hot-dip galvanized steel mesh (1 mm wire, 19x19 mm eyelet) attached to facade dowels (KDS) 10 mm from the insulation. Plasters were applied through the mesh using mortar pumps for efficiency. Approximate layer distribution: KAM-R (1/10 to 1/8), NHL-2 (2/3), NHL-1 (1/3). Final plaster thickness: 25–30 mm.

Sakret has also developed a formulation for **KAM-R**, a coarser plaster with an aggregate size of up to 2 mm. It offers enhanced filling capacity and can be used both as a base coat in thick-coat plaster systems and as a finish coat, depending on the application.

SAKRET KFF lime paint (calcium hydroxide, small amounts of organic additives, linseed oil, water) was used on thick-plaster system. Lime paint is known for its "cloud effect" appearance when wet, is highly breathable, and forms no film. It ages evenly and gracefully.

The main component of the **thin-plaster system** studied here is the mineral plaster SAKRET KAM-R. This factory-produced mixture consists of white Portland cement, calcium hydroxide, organic and inorganic additives for adhesion and workability, and sieved sand (grain size up to 1 mm). It has previously been used in ETICS on historic buildings. Reinforcement is achieved with two layers of alkali-resistant fibreglass mesh (160 g/m², mesh size 4x5 mm). The double-mesh reinforcement is essential in mineral ETICS (without organic topcoat), as it better manages stress arising during curing and use, thus preventing cracking. The finish coat was also applied with KAM-R (approx. 2 mm), finished with a damp-sponge float. The product can also be sprayed for various textures. The total thickness of the thin-layer plaster system is approximately 10 mm. SAKRET KS EXTERIOR silicate paint (potassium silicate solution, organic additives, water) was used on the thin-plaster system. Silicate paint produces a highly durable, breathable, matte mineral surface suitable for plaster, brick, stone, and concrete. Like lime paint, it forms no film and is usually suitable for restoration.

Two **insulation installation approaches** can be used:

1. Adhesive bonding of the insulation to the facade using SAKRET KAM-R mortar, combined with mechanical fixings (facade dowels).
2. A "hanging" system, where the insulation is fixed exclusively with special facade dowels. This solution, widely used in Scandinavia and Germany, allows the system to function as a quasi-independent "shell," less affected by building movement. It still ensures airtightness between the insulation and the supporting wall, which is essential for insulation performance. Additionally, the "hanging" system is easier to dismantle, allowing the insulation to be reused. Only dowel holes remain in the historic substrate, with no adhesive to remove.

On the test wall studied in the project, the **replicated cornices** were also prototyped.

- On thick plaster system they were made of precast lightweight concrete (SAKRET LC). SAKRET LC consists of cement, additives, and foamglass granules (max. 5 mm). The hardened mortar has a density of ~780 g/dm³ and compressive strength of 5

MPa. With rather low thermal conductivity (λ = 0.17 W/(m*K)), its lighter weight reduces vertical load on the plaster. Elements were precast in SAKRET's factory and installed using foam and dowels anchored to the masonry. Surfaces were finished with KAM-R and painted with silicate paint.

- On thin-plaster system, XPS cornices were used. The elements were cut to shape, adhered with PU foam, and fixed with KEW TSBD dowels. Cornices glued to plaster surface and fixed with dowels. Surfaces were finished with KAM-R and painted with silicate paint.

Top surfaces exposed to rainfall can be sealed with mineral waterproofing to prolong durability.

Grooves/panel impressions are often featured in the Stalinist apartment building archetype which mimic block or brickwork, especially at corners. These were recreated on the test wall on the thin-plaster system by milling grooves into the insulation and reinforcing them during plastering with PVC profiles with fibglass mesh, ensuring crack resistance and straight lines. Special joint-profile products are available on the market for more complex shapes.

The typical **surface finish** was a slightly rustic float finish created using plaster with grain size up to 1 mm. Coarser plasters (e.g. SAKRET LHM-2) can also be used. Finishes were applied with standard tools (PU float, rubber float, felt float). On the test wall, the plaster was dampened after partial curing and smoothed using a porous rubber float.

In addition to a plaster intended for full-surface rendering, Sakret also started developing a fine-textured, skim coat-type plaster designed for the restoration of historically smooth finishes and decorative architectural ornamentation.

Both systems can be combined with **hydrophobation**. SAKRET HF (water dispersion of siloxane and silicone resin) was used in current study on selected samples and splash zone of the outdoor test wall.

1.3 Structure of the deliverable

To give an overview of the hygrothermal performance of the proposed ETICS solutions, the main parts of the study and the deliverable are:

1) Material level studies:
    a. Measurement of hygrothermal properties of the plasters to create a material file for modelling.
    b. Measurement of frost damage onset threshold to use as a performance criterion.
2) Reference measurements conducted on component level:
    a. Outdoor test wall subjected to real climate: combinations of insulation materials, plaster systems and orientations are subjected to real climate since summer of 2024 with the aim to directly compare them between each other and gather reference data for modelling.
    b. Climate chamber study on ETICS mockups: the samples are subjected to varied and increasingly extreme conditions to determine the response of the systems and gather reference data for modelling.
3) Hygrothermal modelling:

a. Comparison of modelling and measurement results to assess the accuracy and reliability of the hygrothermal model.
b. Assessment of long-term durability based on critical boundary conditions.

The specific methods of the studies are provided under the respective chapters.

2. Hygrothermal properties and frost resistance of plasters

2.1 Introduction

Full scale outdoor test walls provide valuable information about the long-term performance of renovation systems under real climatic exposure. However, such experiments require significant time and resources and can only investigate a limited number of material combinations. Hygrothermal modelling offers a complementary approach by enabling the assessment of numerous design alternatives and exposure scenarios before selecting the most promising systems for experimental validation. The development of reliable hygrothermal material models requires experimental data describing heat transport, moisture storage, and moisture transport within the investigated materials. Therefore, a comprehensive laboratory characterisation programme was carried out for the studied historic plasters.

This chapter presents the experimentally determined material properties and material functions used for subsequent hygrothermal simulations. The experimental programme included determination of density and porosity, thermal conductivity, water absorption, drying behaviour, water vapour permeability, and moisture retention characteristics. To characterise moisture storage behaviour over the full moisture range, the moisture retention curve was constructed from desiccator, pressure plate and dew point psychrometer measurements.

The collected experimental data were subsequently used to calibrate the material functions required for hygrothermal simulations, including vapour transport, liquid transport and thermal conductivity functions. The resulting material descriptions form the basis for numerical modelling of heat and moisture transfer in the developed historic plaster-based renovation systems.

Frost resistance was evaluated using repeated freeze-thaw cycling combined with ultrasonic pulse velocity measurements. Complementary water uptake testing was performed to assess freeze-thaw induced changes in capillary water absorption behaviour. The selected moisture levels for frost testing were derived from the measured moisture retention functions, capillary water uptake characteristics and vacuum saturation limits, allowing the influence of moisture content on frost durability to be assessed.

2.2 Methods

The experimental programme consisted of a series of thermal, hygric and durability tests conducted on the investigated materials. An overview of the applied methods is given in Table 2.

Table 2: Summary of the experimental program and investigated materials.

	KAM-R	NHL-1	NHL-2	WFB	PF
Frost Resistance	X	X	X		
Thermal Conductivity, *TPS*	X	X	X	X	X
Thermal Conductivity, *Heat Flow Meter*				X	X
Bulk Density	X	X	X	X	X
Porosity	X	X	X	X	
MRC, *desiccator*	X	X	X		
MRC, *psychrometer*	X	X	X		
MRC, *pressure plate*	X	X	X		
Vapour Diffusivity	X	X	X	X	X
Water Uptake	X	X	X	X	
Drying	X	X	X		

2.2.1 Studied materials

Three plaster materials developed by Sakret within the HeriTACE project were investigated: KAM-R, NHL-1 and NHL-2. The materials were designed for use in historic plaster-based external thermal insulation systems intended for the renovation of historic buildings.

KAM-R is a commercially available lime-cement plaster. It consists of white Portland cement, lime, polymers, microfibres, graded quartz sand and mineral fillers. In addition, the material contains a mild hydrophobic additive to reduce liquid water uptake.

NHL-1 and **NHL-2** were developed specifically for the HeriTACE project as components of a thick mineral plaster system. Both materials are based on natural hydraulic lime (NHL 3.5) with a small addition of white Portland cement (approximately 3 mass%), adhesion-promoting polymers and graded quartz sand. NHL-2 functions as the base render, while NHL-1 serves as the finishing render. Although intended to be used together as a single plaster system, the two materials were characterised separately to determine the material properties of each layer individually. This approach enables their representation as distinct layers in hygrothermal simulations and allows layer-specific material functions to be assigned within the numerical model. Their compositions are essentially identical, with the primary difference being the aggregate grading and resulting particle size distribution.

Two insulation materials were investigated in more detail: wood fibre insulation board (Steico Special Dry) and phenolic foam insulation board (Kingspan Kooltherm K5).

Steico Special Dry (WFB) is a rigid wood fibre insulation board manufactured from PEFC-certified wood fibres and containing polyurethane resin and paraffin wax additives. In contrast to phenolic foam, the material possesses an open pore structure and a low water vapour diffusion resistance factor (declared μ ≈ 3), allowing efficient vapour transport through the material. Surface treatment with paraffin wax provides a degree of water repellency while maintaining vapour permeability. Owing to its hygroscopic and porous structure, the wood fibre board can store and redistribute significant amounts of moisture.

Kingspan Kooltherm K5 (PF) is a rigid phenolic foam insulation board characterised by a fine closed-cell pore structure. The insulation core is fibre-free and laminated on both sides with a mineral fleece facing. Phenolic foam insulation materials are generally characterised by relatively high water vapour diffusion resistance compared to mineral-based building materials. Due to its closed-cell structure, Kooltherm K5 exhibits limited moisture storage capacity and low liquid moisture transport.

2.2.2 Frost resistance

Frost resistance is one of the most important properties of external plasters, especially in northern climates. Repeated freezing and thawing of porous building materials under saturated conditions progressively weakens the materials and reduces the service life (Ingham, 2005). Therefore, it is necessary for external plaster to be designed to endure a large number of freeze-thaw cycles throughout their service life.

Frost resistance is commonly evaluated using standardized laboratory tests, such as visual assessment, mass loss measurements, and destructive mechanical testing, all after a certain number of freeze-thaw cycles have been performed e.g. EN 12371:2010 for natural stone and EN 772-18:2011 for calcium silicate masonry. For concrete and natural stone, freeze-thaw damage is often inferred from changes in dynamic elastic properties measured by resonance, dilatometry or ultrasonic transit time, based on EN 12504-4:2021. However, these tests have been designed for concrete and natural stone and therefore are insensitive to early microstructural damage in thin plasters, which could already affect the performance and long-term durability. Ultrasonic pulse velocity testing provides a non-destructive means to assess internal changes in mineral materials and has been widely applied in concrete research as well as other mineral materials (Feng et al., 2019; Karaiskos et al., 2015). Changes in ultrasonic pulse velocity and signal attenuation are linked to stiffness variations and crack development, suggesting potential for early freeze-thaw damage detection (Naik et al., 2003). Its application to thin plaster layers remains limited and requires careful selection of measurement configuration and interpretation.

All specimens were prepared and cured under laboratory conditions (≈22 °C, 50% RH). The plasters were mixed according to their prescribed formulations and cast as flat layers with a uniform thickness of 21 mm. Individual 100 × 100 mm specimens were formed by pressing a metal cutting frame into the fresh plaster, ensuring that all specimens originated from the same plaster bed and no damage was caused while cutting the specimens out after curing (Figure 8). For each material, two molds were cast from a single batch to minimize mixing-related variability. The specimens were then air-cured under stable laboratory conditions for approximately one year prior to testing.

Figure 8: Left: Steel mold used to cut out plaster specimens. Right: KAM-R specimens after drying

Prior to freeze-thaw exposure, the specimens were conditioned to predefined moisture states representing different degrees of saturation. Four target moisture levels, calculated from mass-based moisture saturation, were selected based on water retention curves and capillary saturation limits: full saturation (≈100%) achieved by vacuum saturation (

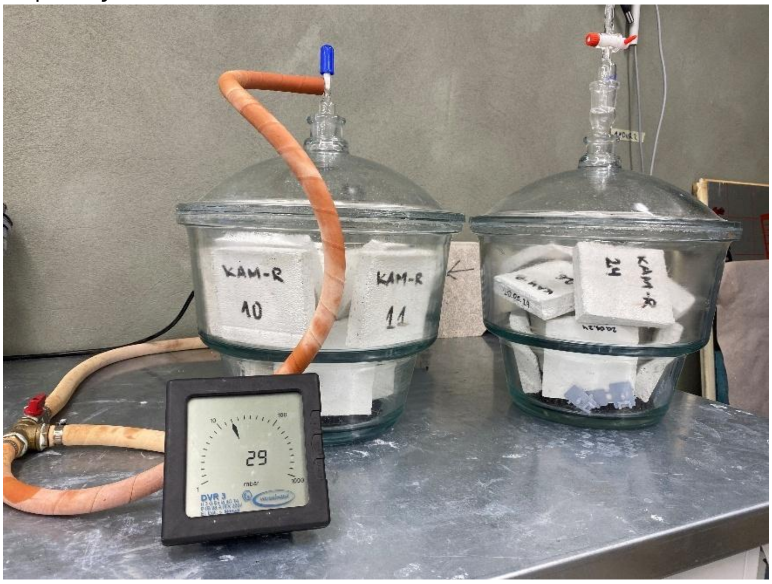

Figure 9), capillary saturation at ≈70%, equilibrium moisture content at 97% RH (≈30%), and an intermediate level of ≈45%. Moisture conditioning involved vacuum saturation followed by controlled drying to the target levels in a ventilated chamber to ensure homogeneous moisture distribution and reproducible freeze-thaw exposure.

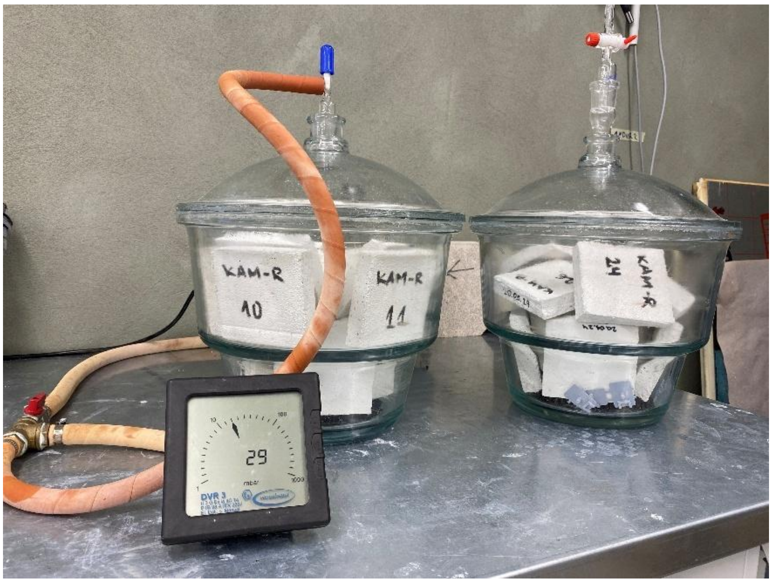

Figure 9: Vacuum saturation procedure of KAM-R specimens

Freeze-thaw cycling was conducted in a climate chamber with temperature monitored by Pt1000 sensors in the air and within dedicated plaster samples. In the first experimental stage, four specimens per moisture level underwent 10 freeze-thaw cycles down to -20°C (10 FTC), with three specimens per moisture level in a parallel reference group without cycling (0 FTC) stored at +3 °C to distinguish freeze-thaw damage from moisture induced curing. Each 24-hour cycle consisted of a slow cooling and freezing phase and a rapid heating and thawing phase (Figure 10). After cycling, all specimens were dried at +43 °C in a ventilated cabinet until mass stabilization prior to further testing.

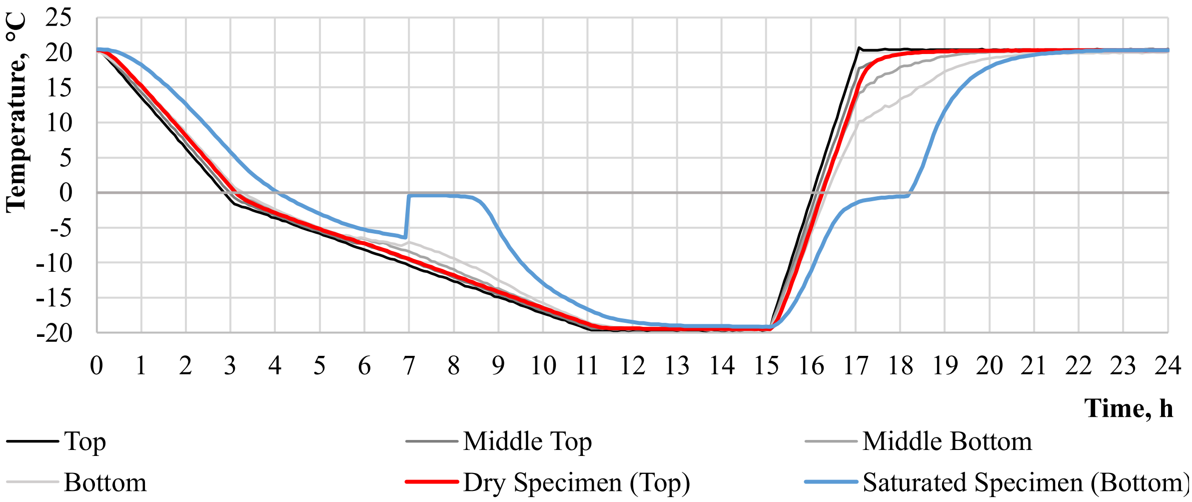

Figure 10: Temperature profile of a single freeze-thaw cycle, recorded using four air sensors (grey) and two sensors embedded in plaster specimens (red and blue) at different moisture levels. The blue curve reflects the embedded sensor in fully saturated specimen, small plateau around 7-9 h is caused by latent heat during freezing.

Ultrasonic pulse velocity (UPV) was measured with a Proceq Pundit Lab (+) using coupling gel. Two transducer types were used: Proceq 500 kHz flat contact transducers for through-thickness measurements and Proceq 54 kHz exponential transducers for in-plane measurements. All measurements were taken in the dry state before and after freeze-thaw cycling to avoid moisture effects. Through-thickness measurements captured longitudinal bulk wave transmission across the 21 mm thickness using 500 kHz transducers placed at the center or, when coupling was difficult, at a marked alternative point (Figure 11, Figure 12). A longer transmission path was later introduced to improve resolution as the short path approached equipment limits. In-plane measurements were performed over a 100 mm path using 54 kHz transducers placed on opposite specimen edges, with two predefined ultrasonic wave propagation trajectories in two orthogonal directions (Figure 11). Because the specimens act as thin plates, wave propagation along the 100 mm path was dominated by guided plate waves, and group-velocity behaviour was estimated using material parameters (ρ = 1550 kg/m³, E= 9.5 GPa, ν = 0.1, d = 21 mm) to confirm suitability of the chosen frequency and path.

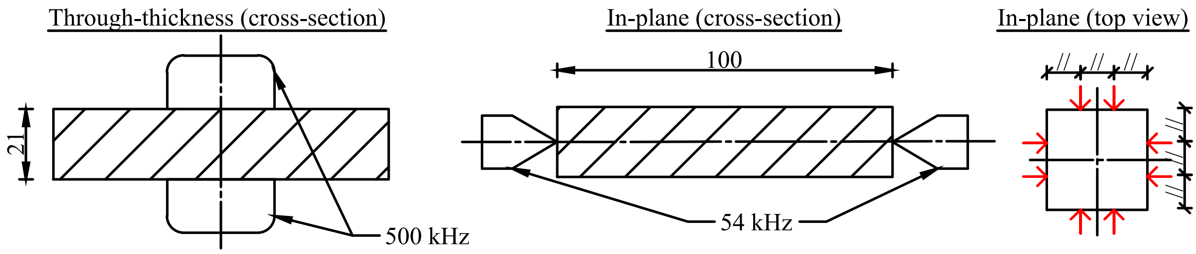

Figure 11: UPV measurement transducer placement.

Figure 12: UPV through-thickness test setup (left) and in-plane test setup (right).

After ultrasonic testing, complementary tests were conducted to support the interpretation of UPV results and to validate freeze-thaw induced damage. A visual assessment was first performed to identify surface cracking or other visible deterioration. A 48-hour water absorption test was then conducted. Dried specimens were placed with the 100 × 100 mm face surface in 5 mm deep water, and mass was recorded at predefined intervals to obtain water uptake curves. The evaluation followed the general principles of standardized capillary uptake testing, while the specimen geometry and test setup were adapted for this study.

Damage indicator Ω was used to analyze UPV measurements and to quantify microstructural degradation (Feng et al., 2019).

$$\Omega = 1 - \left(\frac{E_0}{E}\right) = 1 - \left(\frac{t_0}{t}\right)^2$$

Here, E_0 and E are the dynamic modulus of elasticity before and after freeze-thaw cycling, t_0 is the initial pulse travel time of the dry specimen, and t is the travel time after cycling with curing correction. To separate freeze-thaw damage from moisture-related curing, travel time changes measured in reference specimens at the same moisture levels were subtracted from the cycled specimens. Although no established Ω threshold exists for lime-based plasters, a value of 0.3 was used as an indicative limit based on durability criteria for concrete and natural stone, where a 30% reduction in dynamic modulus of elasticity is typically associated with frost damage based on EN 12371:2010. For in-plane measurements, four predefined points were used per specimen. Mean ultrasonic pulse velocity and its variation were calculated to assess spatial variability and crack-induced heterogeneity, the damage indicator Ω was derived accordingly.

Water absorption behavior was evaluated during 48 h partial immersion tests. The absorption coefficient A_w (kg/(m^2·√s)) was obtained from the initial linear sorption phase following. Reference and cycled specimens were compared to assess frost-induced changes in pore connectivity and liquid transport

2.2.3 Thermal properties

The thermal conductivity of the investigated materials was determined using two methods: the **transient plane source (TPS) method** and the **heat flow meter (HFM) method**. TPS measurements were performed on all plaster and insulation materials, while HFM measurements were additionally carried out on the insulation materials.

TPS measurements were conducted using a Hot Disk TPS2200 thermal constants analyser in accordance with EN ISO 22007-2 (Figure 13 (left)). For the plaster materials, a Kapton 5501 sensor was placed between two oven-dry specimens measuring 100 × 100 × 45 mm. For the insulation materials, a larger Kapton 5599 sensor was positioned between oven-dry 100 mm thick insulation boards. The sensor simultaneously acted as a heat source and temperature sensor, allowing thermal conductivity to be determined from the measured transient temperature response. To account for material heterogeneity, measurements were repeated on different specimen surfaces and the results were averaged.

HFM measurements were performed using a TA Instruments FOX 200 apparatus. The specimens measured 200 × 200 × 40 mm and were conditioned at 23 °C and 50% RH prior to testing. During the measurement, the specimens were placed between two temperature-controlled plates with a temperature difference of 10 °C across the material (Figure 13 (right)). Thermal conductivity was determined from the measured heat flux under steady-state conditions. For the wood fibre board (WFB), measurements were carried out both parallel and perpendicular to the fibre direction to assess the influence of material anisotropy on thermal conductivity.

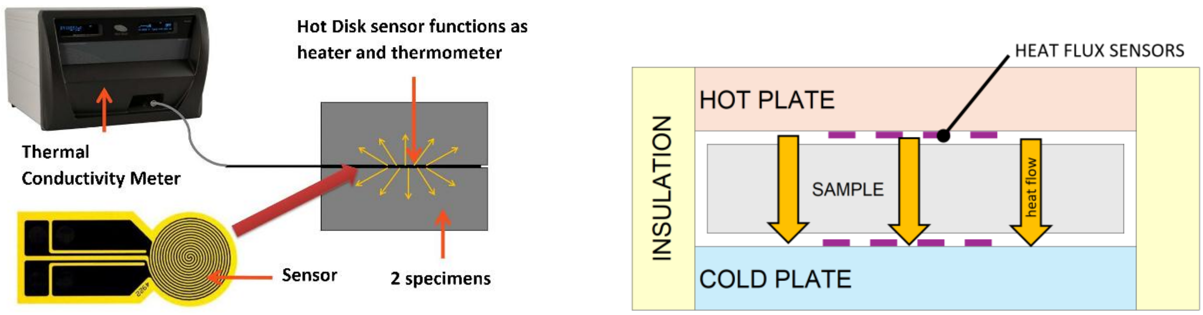

Figure 13: Schematic working principle of the transient plane source (left) and heat flow meter (right) method.

2.2.4 Moisture retention curve

The density and porosity of the investigated materials were determined using methods adapted from EN 772-13:2000 and EN 1936:2006 for the plaster materials and ASTM C1699-09(2015) for the insulation materials. Prior to testing, all specimens were dried to constant mass. Plaster specimens and wood fibre board (WFB) specimens were dried at 43 °C, while phenolic foam (PF) specimens were conditioned in a ventilated chamber at 0% RH. For the insulation materials, bulk density was determined from the dry mass and specimen dimensions measured using a digital calliper. For the plaster materials, apparent bulk density and open porosity were determined using a vacuum saturation procedure. Dry specimens were placed in a vacuum desiccator and saturated with distilled water under vacuum conditions, after which the saturated mass in air and the apparent mass under water were recorded. The same procedure was additionally applied to WFB specimens to determine open porosity. The measured masses were used to calculate apparent bulk density and open porosity according to Archimedes' principle. Porosity measurements were not performed for the phenolic foam insulation due to its predominantly closed-cell pore structure.

The moisture retention behaviour in the hygroscopic range was determined using **the desiccator method** in accordance with EN ISO 12571:2021 with minor modifications (Figure 14). Measurements were performed on 50 × 50 × 5 mm specimens of the plaster materials at a temperature of 23 °C. Prior to testing, the plaster specimens had undergone approximately four months of curing and carbonation under laboratory conditions (23 °C, 50% RH). The specimens were exposed to controlled relative humidity environments generated by saturated salt solutions corresponding to 43% RH (K_2CO_3), 75% RH (NaCl) and 97% RH (K_2SO_4). Both adsorption and desorption paths were investigated by sequentially conditioning the specimens at the selected humidity levels until mass equilibrium was reached. The equilibrium moisture contents obtained at each humidity level were used to construct the hygroscopic portion of the moisture retention curve. To define the upper boundary of the moisture storage function, the moisture content at 100% RH was assumed equal to the vacuum saturation moisture content determined separately using the vacuum saturation procedure.

Figure 14: Desiccator used for hygroscopic moisture retention measurements. The specimens were conditioned above a supersaturated salt solution, while an internal fan provided air circulation to promote uniform relative humidity within the chamber.

The moisture retention behaviour in the overhygroscopic range was determined using a combination of pressure plate and dew point psychrometer measurements at 23 °C.

Pressure plate measurements were performed on 50 × 50 × 5 mm plaster specimens using a 1500F2 15 Bar Pressure Plate Extractor apparatus by Soilmoisture Equipment Corp. in accordance with ASTM C1699-09 (2015) (Figure 15). Prior to testing, the specimens were vacuum saturated and placed on a water-saturated ceramic plate inside a sealed pressure vessel. Kaolin clay was used as a medium to create hydraulic contact between the samples and the ceramic plates, while cellulose film was used to prevent the migration of the clay to the samples. Increasing air pressure was applied above the specimens, forcing water out through the ceramic plate until hydraulic equilibrium was reached. The equilibrium moisture content corresponding to each pressure level was subsequently determined gravimetrically. Measurements were conducted at suction pressures of 43.1, 100, 317 and 658 kPa.

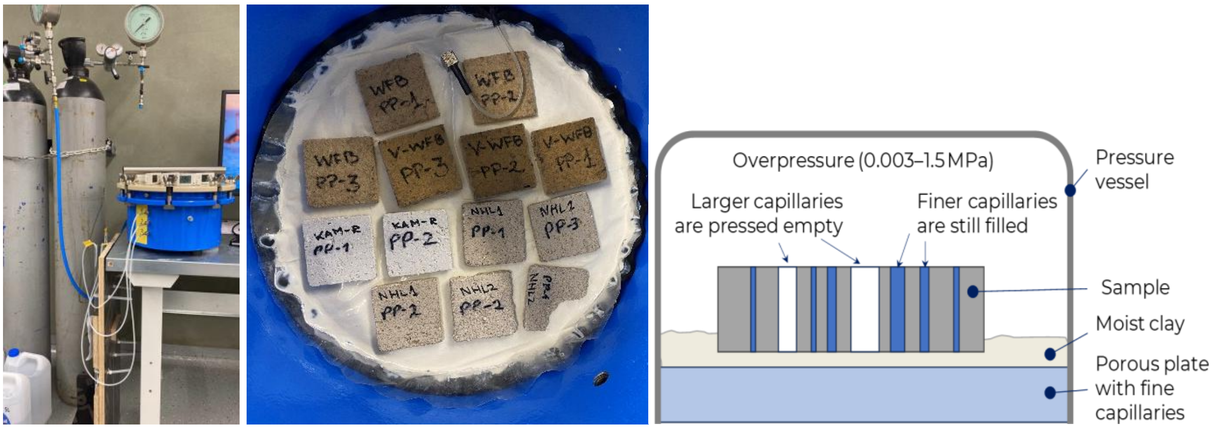

Figure 15: Pressure plate apparatus used for moisture retention measurements (left), specimen arrangement inside the pressure vessel (middle), and schematic illustration of the pressure plate measurement principle (not to scale, right).

For higher suction pressures, a Meter Group WP4C **dew point psychrometer** was used. Measurements were performed on disc-shaped specimens with a diameter of 32 mm and a thickness of approximately 3–5 mm. The method is based on establishing equilibrium between the moisture in the specimen and the water vapour in a sealed measurement chamber. The dew point temperature of the chamber air and the specimen temperature are measured, allowing the corresponding relative humidity and moisture potential to be determined. Specimens were conditioned to different moisture states prior to testing, and the resulting equilibrium moisture contents were combined with the pressure plate and desiccator measurements to construct the complete moisture retention curve.

Figure 16: Dew point psychrometer (Meter Group WP4C) used for moisture retention measurements in the overhygroscopic range (left), gravimetric determination of specimen moisture content (middle), and schematic illustration of the dew point psychrometer measurement principle (right).

2.2.5 Water vapour transfer

Water vapour transmission properties were determined using a modified **cup test** procedure based on the principles of EN ISO 12572:2016 (Figure 17). Measurements were performed on the plaster materials, wood fibre board (WFB) and phenolic foam (PF) specimens. Plaster and phenolic foam specimens measured 65 × 65 × 20 mm, while WFB specimens measured 65 × 65 × 50 mm. Prior to testing, all specimens were dried to constant mass and sealed to plastic cup lids using butyl tape to ensure one-dimensional vapour transport through the specimen. The tests were conducted in a climate chamber maintained at approximately 25 °C. Both dry cup and wet cup measurements were performed. Dry cup conditions were established using LiCl (ca 11% RH) inside the cup and K_2CO_3 (ca 43% RH) in the surrounding chamber. Wet cup conditions were established using K_2SO_4 (ca 97% RH) inside the cup and KCl (ca 84% RH) in the surrounding chamber. Periodic mass measurements were used to determine the steady-state vapour flow through the specimens and to calculate the water vapour diffusion resistance factor (μ). The measurements were performed after approximately four months of curing and ageing under laboratory conditions. The resulting data were used to determine the water vapour diffusion resistance factor (μ) of the materials.

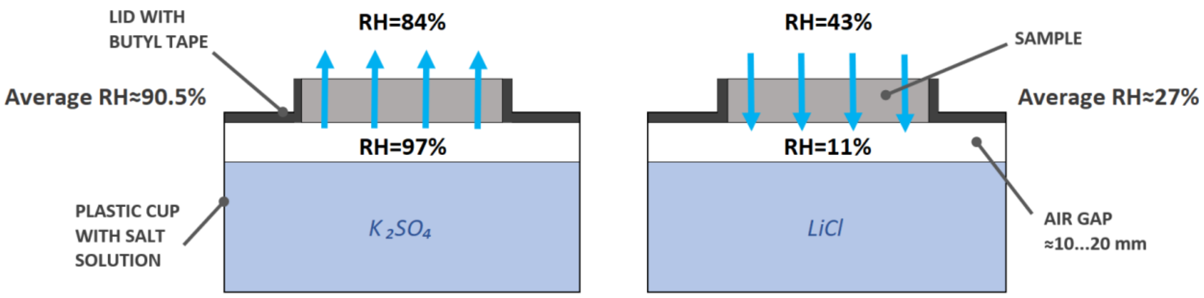

Figure 17: Principle of the wet cup (left) and dry cup (right) methods for determining water vapour transmission properties.

2.2.6 Liquid transfer

Capillary water uptake was determined using a modified test procedure based on the principles of EN ISO 15148. Three specimens measuring 50 × 50 × 50 mm were tested for each material. Prior to testing, the specimens were dried to constant mass and the dimensions were measured. To ensure predominantly one-dimensional water transport, five sides of each specimen were sealed with aluminium foil tape, leaving only the bottom 10 mm exposed (Figure 18). Small openings were left in the upper tape layer to allow the displacement of air from the specimen during water uptake. During the experiment, the specimens were placed in contact with water through their lower surface while maintaining a constant water depth of approximately 5 mm. The increase in specimen mass due to water absorption was monitored gravimetrically at regular intervals during the initial stage of the experiment and subsequently at increasing time intervals until capillary saturation was approached and the mass uptake curve reached a plateau. The measured mass increase was used to determine the water absorption coefficient A_w (kg/(m^2·√s)), which was subsequently used to describe liquid moisture transport within the hygrothermal model.

In addition, water uptake measurements were performed on wood fibre board (WFB) specimens. Due to the hydrophobic treatment of the material, classical capillary rise was not observed; however, the measurements provided information on moisture uptake under direct water contact.

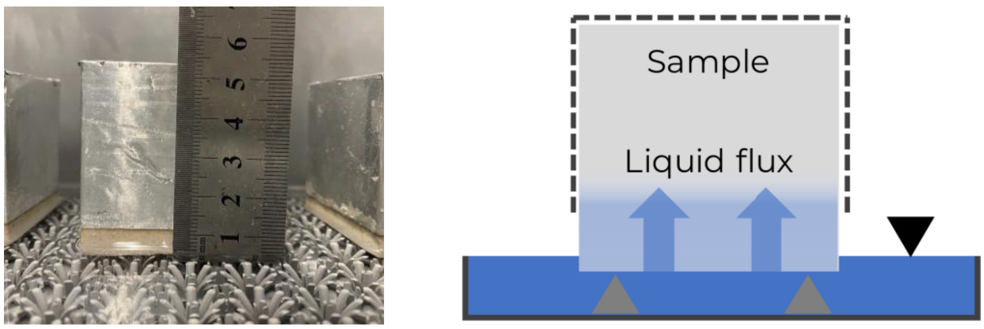

Figure 18: Water uptake experiment showing a sealed plaster specimen in contact with water through its lower surface (left) and a schematic illustration of the test principle and one-dimensional capillary water transport (right).

Drying behaviour was investigated for the plaster materials using a modified procedure based on (Scheffler & Plagge, 2005). Three specimens measuring 50 × 50 × 50 mm were tested for each material. Prior to testing, the specimens were vacuum saturated and subsequently sealed on five sides using vapour-tight tape and 13 mm Armaflex insulation, leaving only one surface exposed for drying. The specimens were placed in a wind tunnel maintained at approximately 23 °C and 50% RH with an air velocity of 1 m/s across the drying surface (Figure 19). During the experiment, specimen mass was recorded periodically to determine moisture loss, while temperature was continuously monitored using sensors installed approximately 10 mm below the drying surface at the interface between the plaster specimen and the Armaflex insulation. Measurements continued until the specimens approached moisture equilibrium with the surrounding environment. The resulting drying curves were used to evaluate the drying characteristics of the materials and to calibrate the liquid transport function used in the hygrothermal material models.

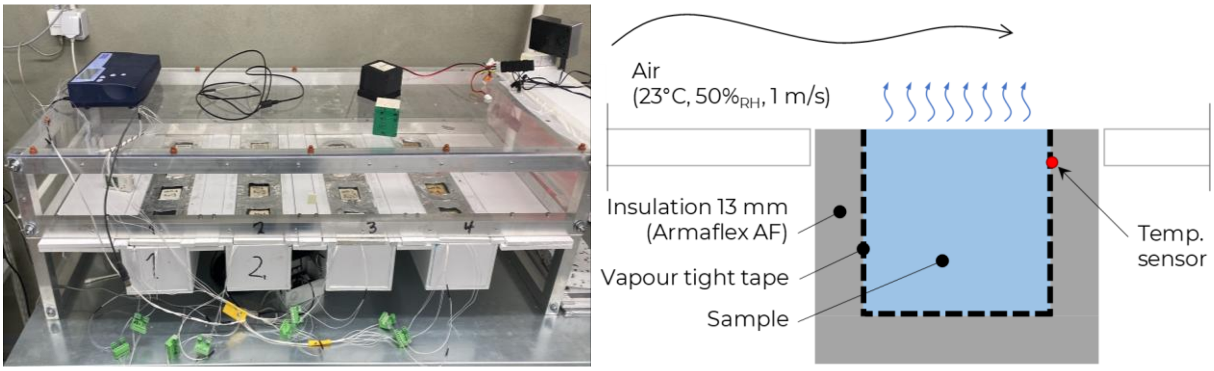

Figure 19: Wind tunnel used for the drying experiments (left) and schematic representation of the specimen configuration used for one-dimensional drying measurements (right). The wind tunnel operated as an exhaust system, with air drawn from left to right across the exposed drying surfaces. Temperature of each specimen was monitored using temperature sensors. The specimens were sealed on five sides using a vapour-tight tape layer covered with Armaflex insulation, leaving only the drying surface exposed to the airflow.

2.2.6.1 Calibration of transfer functions

Based on the laboratory measurements, hygrothermal material models were developed for the three investigated plaster materials. The material functions were calibrated using Material Generator 2 (version 0.8), a software tool developed by IBK TU Dresden. The software was used to generate the initial Delphin material files required for subsequent hygrothermal simulations. These files included the moisture retention curve, water vapour transport function, liquid transport function and a temperature-dependent thermal conductivity function.

The moisture retention function was derived from the combined results of the desiccator, pressure plate and dew point psychrometer measurements. The water vapour transport function was calibrated using the dry cup and wet cup test results, while the liquid transport function was adjusted based on the measured capillary water uptake and drying behaviour. The thermal conductivity function was derived from the measured dry-state thermal conductivity. Moisture dependency was represented using the default linear thermal conductivity model implemented in Delphin (Vogelsang et al., 2013). The resulting material files were subsequently used as input data for the hygrothermal simulations presented in the following chapters.

2.3 Results & discussion

2.3.1 Summary sheets of studied materials

2.3.1.1 Plasters

Table 3 summarises the experimentally determined hygrothermal properties of the investigated plaster materials. In addition to the measured material properties, the calibrated moisture retention and liquid transport functions derived from the laboratory characterisation programme are presented in Figure 20.

Table 3: Measured material properties of the studied plasters (± values denote standard deviation).

Material property	NHL-1 (finishing plaster)	NHL-2 (base plaster)	KAM-R (lime-cement plaster)
Density ρ, kg/m^3	1587 (±22)	1512 (±24)	1513 (±32)
Porosity ψ_{por}, m^3/m^3	0.38 (±0.01)	0.40 (±0.02)	0.40 (±0.01)
Capillary sat. ψ_{cap}, m^3/m^3	0.27 (±0.00)	0.28 (±0.00)	0.26 (±0.00)
Wat. vapour diff. resistance factor $\mu_{11/43}$, -	12.2 (±0.3)	19.0 (±0.2)	15.6 (±0.7)
Wat. vapour diff. resistance factor $\mu_{84/97}$, -	8.3 (±1.5)	10.2 (±1.7)	10.8 (±1.8)
Thermal conductivity λ_{TPS}, W/(m·K)	0.66 (±0.01)	0.86 (±0.01)	0.96 (±0.01)
Water absorption coeff. A_w, kg/(m^2·s$^{0.5}$)	0.068 (±0.002)	0.038 (±0.001)	0.023 (±0.001)

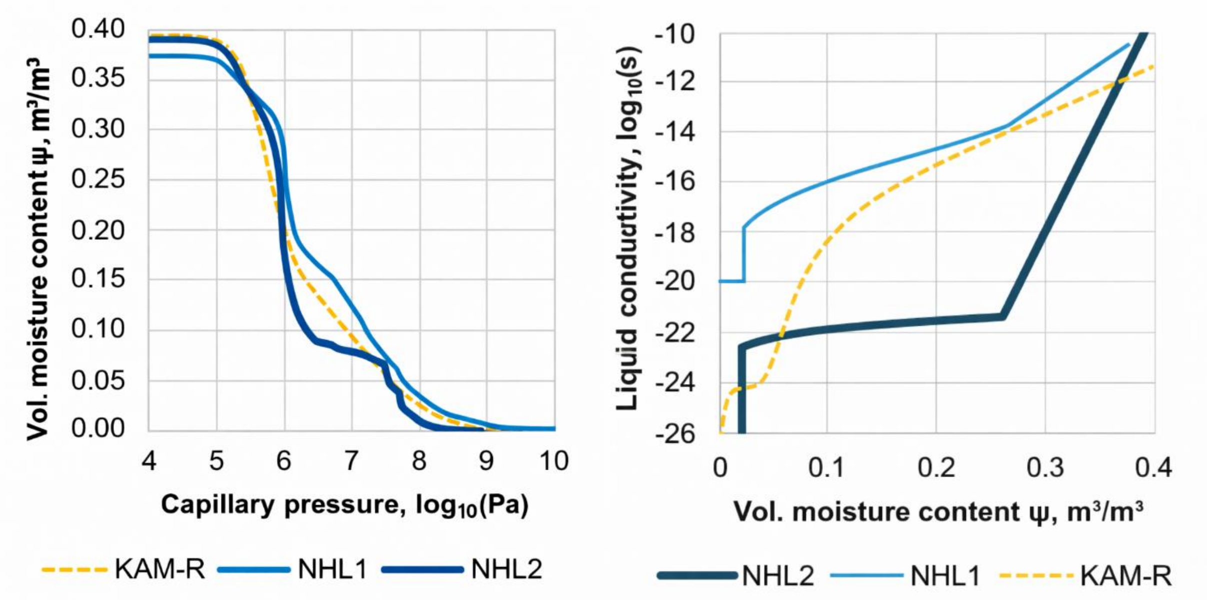

Figure 20: Liquid transport conductivity functions (left) and moisture retention curves (right) calibrated for the investigated plaster materials based on the experimental results.

While the investigated plasters exhibited very similar density, open porosity and capillary saturation moisture contents, noticeable differences were observed in their moisture retention behaviour. NHL-2 exhibited lower moisture contents than NHL-1 and KAM-R throughout most of the overhygroscopic moisture range. This difference persisted from the onset of the overhygroscopic region up to capillary saturation, where the moisture contents of all three plasters approached similar values. Given that NHL-1 and NHL-2 were based on essentially the same formulation and differed primarily in aggregate particle size, the results suggest that aggregate grading influenced the pore size distribution and consequently the moisture storage characteristics of the plaster.

2.3.1.2 Insulation

Table 4 summarises the experimentally determined hygrothermal properties of the investigated insulation materials. Thermal conductivity values are reported for both measurement methods employed in this study: the transient plane source (TPS) method and the heat flow meter (HFM) method. For the wood fibre board, HFM measurements were performed both perpendicular and parallel to the board plane in order to capture the anisotropic thermal behaviour of the material. The perpendicular (⊥) direction corresponds to the orientation of the board in its intended wall application, whereas the parallel (∥) direction represents heat flow within the plane of the board.

Table 4: Material properties of the studied insulation materials (± values denote standard deviation).

Material property	Wood Fibre Board	Phenolic Foam
Density ρ, kg/m^3	133 (±7)	32 (±4)
Porosity ψ_{por}, m^3/m^3	0.93 (±0.02)	-
Wat. vapour diff. resistance factor $\mu_{11/43}$, -	1.8 (±0.1)	80.5 (±11.7)
Wat. vapour diff. resistance factor $\mu_{84/97}$, -	1.5 (±0.2)	2.9 (±0.3)
Water absorption coeff. A_w, kg/(m^2·s$^{0.5}$)	0.022 (±0.003)	-
Thermal conductivity λ_{TPS}, W/(m·K)	0.052 (±0.009)	0.018 (±0.001)
Thermal conductivity $\lambda_{HFM\perp}$, W/(m·K)	0.043 (±0.0004)	0.019 (±0.0001)
Thermal conductivity $\lambda_{HFM\parallel}$, W/(m·K)	0.064 (±0.002)	-

2.3.2 Frost resistance

Clear damage after 10 freeze-thaw cycles was detected only at 100% saturation level with all tested plasters (Figure 21). After freeze-thaw cycling, fine surface cracks appeared on the mold-contact face of two fully saturated NHL1 specimens, while the rest of the specimens had no visible damage on any of the surfaces. Based on UPV testing, damage indicator Ω ranged from 0.6 to 0.85 for 100% saturation specimens, well above the 0.3 threshold. Slight microcracking was evident in NHL2 specimens cycled at 70% saturation, based on increase in Ω and Aw (Figure 21), although Ω did not exceed 0.3, systematic trends indicated the onset of early frost damage.

2.3.2.1 Ultrasonic pulse method

Through-thickness ultrasonic pulse velocities (UPV) increased by about 15 to 20% after moisture conditioning, cycling and drying, except for severely damaged fully saturated and cycled specimens, demonstrating continued curing and justifying the use of reference groups to isolate freeze-thaw damage. After freeze-thaw cycling, fine surface cracks appeared on the mold-contact face of two fully saturated NHL1 specimens. All fully saturated NHL1 specimens showed clear deviations in ultrasonic response. The cracked specimens had the lowest in-plane velocities, around 1250 m/s, while the visually intact but still damaged specimens reached about 1750 m/s (Figure 22). Both groups differed from the remaining NHL1 specimens, which showed velocities around 2670 ± 85 m/s. No through-thickness ultrasonic signal was detected across the 21 mm thickness in the cracked NHL1 specimens when using 500 kHz transducers. A signal was still detected in visually intact fully saturated NHL1 specimens, with velocities around 1700 m/s. Fully saturated and cycled NHL2 and KAM-R specimens also showed no transmitted signal, despite the absence of visible surface damage. In-plane measurements revealed very low velocities for fully saturated NHL2 specimens, around 1120 m/s, indicating internal microcracking. Spatial variability ranged from 7 to 13% for NHL1, 4 to 12% for NHL2, and about 10% for KAM-R.

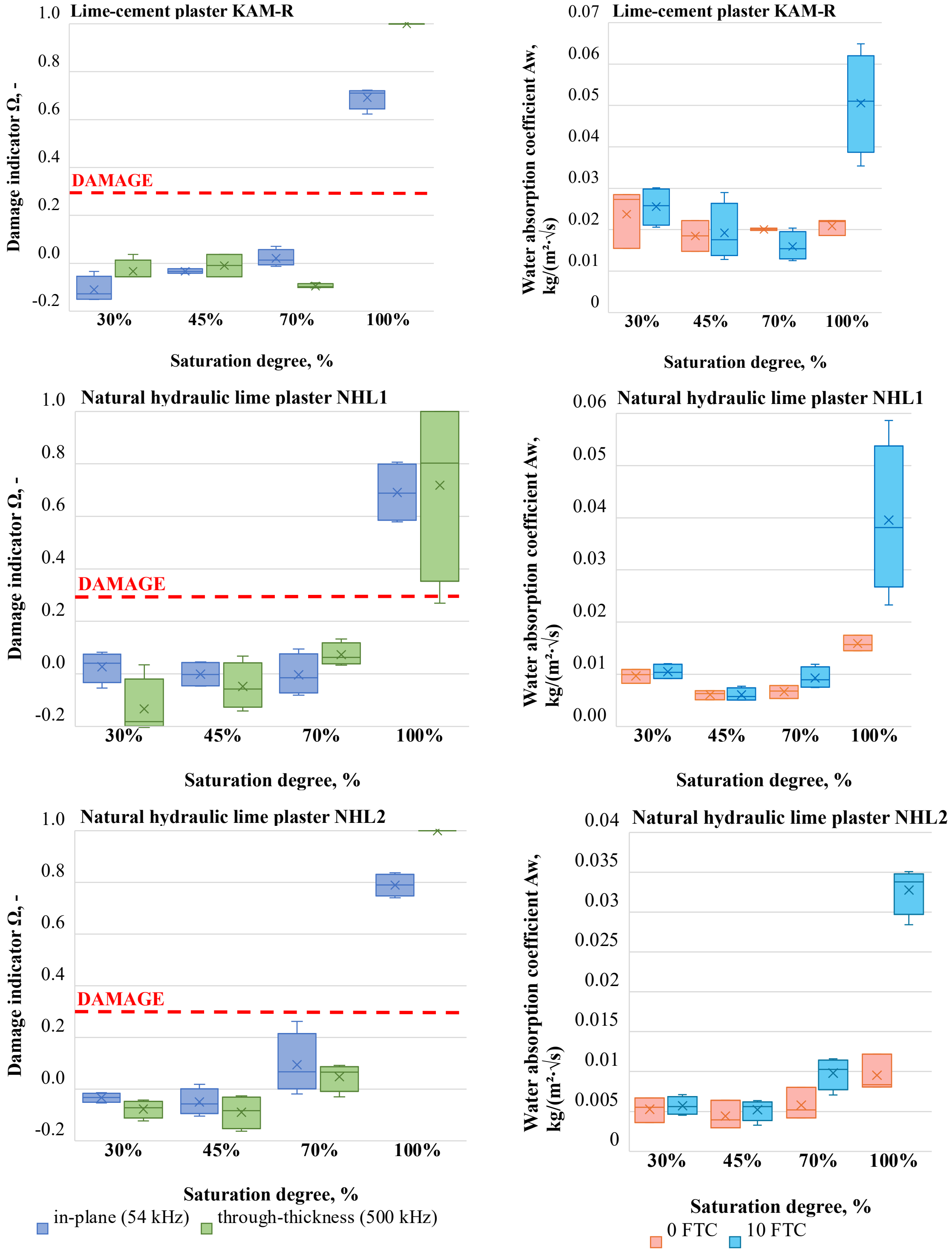

Figure 21: Left column: damage indicator Ω for KAM-R, NHL1 and NHL2 specimens at different saturation levels during freeze-thaw cycling, derived from ultrasonic measurements performed in-plane (100 mm path, 54 kHz transducers) and through the specimen thickness (21 mm path, 500 kHz transducers). Right column: capillary water absorption rates A_w (kg/(m²·√s)) for cycled (10 FTC) and uncycled (0FTC) specimens.

2.3.2.2 Water uptake of F/T cycled samples

Water absorption and ultrasonic pulse velocity test results were in agreement between each other, confirming that the water absorption test can be used as an independent validation method. Clear difference in water absorption can be observed on the graphs between damaged specimens and all the other specimens, suggesting the formation of internal microcracks that allowed for faster water uptake (Figure 22). NHL1 and KAM-R damaged samples showed wide variation in water uptake coefficient, while variations for NHL2 damaged specimens were minor (Figure 21).

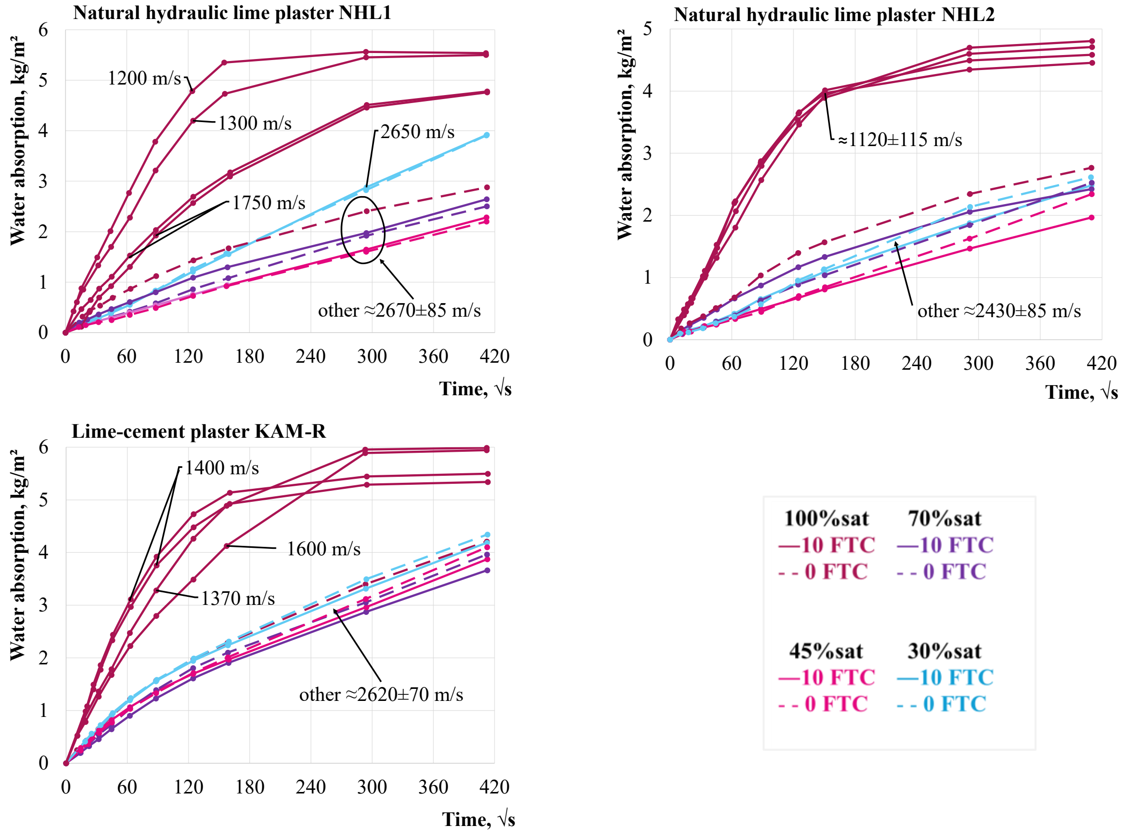

Figure 22: Water absorption curves of conditioned cycled (10 FTC) and uncycled reference (0 FTC) specimens for KAM-R, NHL1 and NHL2. Curves represent group mean values, except for fully saturated cycled specimens, for which individual curves are shown. In-plane UPV values are reported for all specimens, as individual values for damaged fully saturated specimens and as group mean values for the remaining saturation groups.

2.3.2.3 Conclusions

Freeze-thaw cycling caused measurable microstructural damage in all plaster types. Visible cracking occurred only in some of the fully saturated NHL1 specimens, while ultrasonic measurements revealed internal cracking in visually intact specimens. High-frequency through-thickness signals were lost due to scattering, whereas low-frequency in-plane measurements remained quantifiable. Capillary absorption trends aligned with ultrasonic indicators, confirming its value as an independent validation method. The unfrozen reference sets of samples allowed to separate frost damage from ongoing curing, and low-frequency guided waves were preferred as an effective non-destructive technique for this setup.

3. Component level experiments

3.1 Introduction

To evaluate the performance of the novel plaster systems in combination with insulation, two experimental setups were used: a free-standing outdoor test wall and several wall-section specimens mounted in a climate chamber. The **outdoor test wall** was exposed to real weather conditions without an indoor moisture load. Besides visual evaluation over two winters, sensors installed in the wall sections continuously measured temperature and relative humidity (RH), making it possible to compare the performance of different systems and orientations.

In addition to the outdoor measurements, smaller specimens representing different wall sections were tested in a **climate chamber** under controlled conditions. The climate chamber experiment made it possible to expose the specimens to identical climate cycles and to study the moisture behaviour of the materials in a more controlled way. The relatively small size of the specimens enabled gravimetric measurements throughout the experimental programme.

The climate chamber experiment lasted from June 2025 until the end of December 2025. The free-standing test wall was erected in spring 2024, and measurements are ongoing. The results from both experiments were used for the calibration and validation of hygrothermal models.

3.2 Methods

3.2.1 Freestanding outdoor test wall

3.2.1.1 Test setup

The test wall demonstrates eight ETICS solutions and one ventilated solution for plastered masonry walls, combining four insulation materials with both thin-layer and thick-layer plaster systems (Talvik et al., 2025). The aim was to demonstrate buildability and study the performance of combinations of historic façade plasters and modern insulation materials under real environmental conditions.

Figure 23: The freestanding wall to test the durability and hygrothermal performance of the historical plaster systems on top of insulation materials.

Besides conventional bonded systems, a mechanically fixed "hanging" system, in which the insulation is attached only with façade dowels, was demonstrated. This approach is especially relevant for historic substrates, as it reduces irreversible intervention: after dismantling, only anchor holes remain, with no adhesive residues on the original plaster or masonry. It also allows the insulation to function as a more independent outer shell, reducing sensitivity to structural movements and improving the potential for future reuse.

The thin-layer systems used SAKRET KAM-R with two layers of fibreglass mesh, creating a reinforced mineral plaster build-up of approximately 10 mm. The double mesh is an important feature, as it helps distribute curing and service stresses and reduces the risk of cracking in mineral ETICS. The thick-layer systems, with a total plaster thickness of 25–30 mm, used project-specifically developed NHL-1 and NHL-2 hydraulic lime-based plasters reinforced with hot-dip galvanised steel mesh. The lime-based solution offers improved compatibility with historic masonry and a more authentic architectural appearance.

To demonstrate the possibility of recreating simpler details of the original façade, several cornices and grooves were introduced into the façade setup. Lightweight cornice elements made from XPS (for the phenolic foam and EPS sections) and expanded-glass lightweight concrete (for the mineral wool and wood fibre board sections) allowed traditional façade details to be recreated without excessive load on the plaster system.

Figure 24: Insulated façade under scaffold sheeting before plastering (left); steel mesh for the thick plaster system and a mesh fastener on top of an insulation anchor (center); application of lime-cement (L/C) plaster and reinforcement profiles at the XPS corners on top of the EPS insulation (right).

3.2.1.1 Instrumentation

To monitor the hygrothermal behaviour of the test wall, 30 digital temperature and relative humidity sensors (Sensirion SHT35) were installed within the wall sections during construction (Figure 25, left). Data were collected at 10-second intervals using tailor-made Arduino-based dataloggers and later processed into 15-minute averages. All sensors were new, factory-calibrated, and additionally checked before installation in a constant temperature and humidity chamber. Most sensors were positioned at the interface between the plaster system and the insulation material, while additional sensors were installed at the boundary between the structural masonry and insulation layer and behind the façade plaster system in the hydrophobically treated zone.

Outdoor climate conditions were measured on-site next to the test wall (Figure 25, right). Conventional meteorological parameters (temperature, RH, wind velocity, wind direction, air pressure, and vertical rain) were recorded using an Ecowitt WS69 weather station. Direct and diffuse solar radiation were measured separately using instruments installed on the roof of an adjacent building (Talvik et al., 2025).

In addition to the conventional weather data, as the wall setup with thick plaster systems is especially sensitive to wind-driven rain loads, two identical direct wind-driven rain measurement devices were developed and installed next to the test wall, facing south and north, respectively. Each device was based on an Ecowitt WH40 rain collector, modified by replacing the collection bowl with a vertical PVC rain screen measuring 0.2 m × 0.6 m. The performance of these screens and their comparison with WDR loads calculated from the on-site weather station using the formulas given in EN ISO 15927-3 are described in detail in (Talvik et al., 2026).

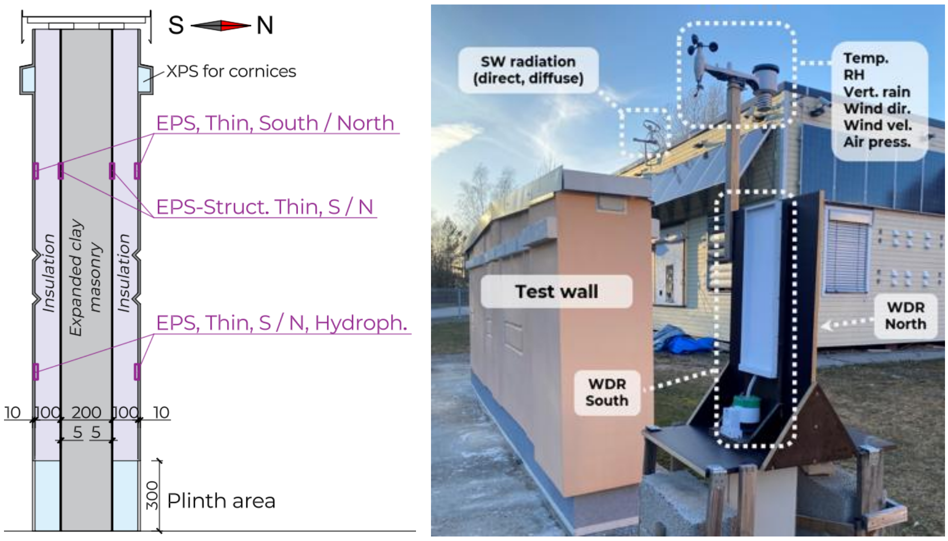

Figure 25: Sensor locations on the cross section with EPS insulation and thin plaster (left); meteorological station setup for measuring WDR and other climatic parameters (right). (Talvik et al., 2025)

3.2.1.1 Modelling local climate conditions with CFD

Computational Fluid Dynamics (CFD) were used to simulate WDR distribution around the experimental site. Simulation was conducted, using the Eulerian Multiphase approach within the OpenFOAM environment, utilizing the windDrivenRainFoam solver developed by (Kubilay et al., 2013). The simulations were performed on the High Performance Computing Centre of TalTech and were based on a 3D model that included the test wall, WDR measurement screens, weather station, and surrounding buildings (Figure 26). The CFD model was used to determine the differences in Global Catch Ratio between test wall surface and adjacend WDR collection screen. This was achieved by calculating catch ratios for different raindrop sizes and combining the results using Best's raindrop size distribution.

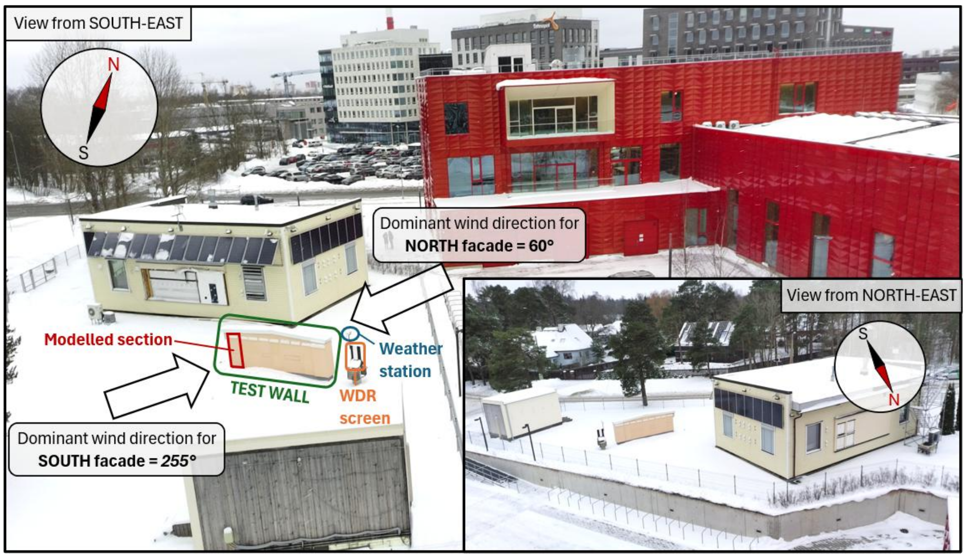

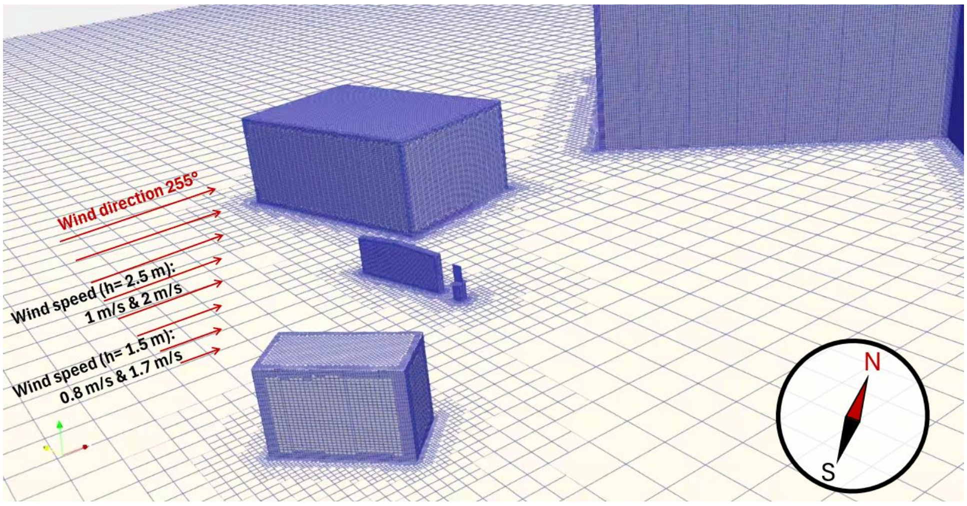

Figure 26: Situation around the test wall and location of direct WDR measurement screens and local weather station (above), CFD domain geometry and mesh topology (3,1M cells) with wind direction and velocity combinations modelled (below). (Talvik et al., 2026)

3.2.2 Climate chamber experiment

3.2.2.1 Test setup

The experiment took place in a climate chamber with adjustable temperature control and humidification. The test samples (see Figure 27, left) consisted of a plaster system along with an insulation layer, the exposed surface was 300 x 300 mm, while samples were sealed laterally and from the rear. The studied combinations are summarized in Table 5. All in all, 2 different plasters (10-13 mm lime-cement (LC) and 30 mm natural hydraulic lime (NHL)) were used on 4 insulation materials (expanded polystyrene (EPS), phenolic foam (PF), wood fibreboard (WFB), mineral wool (MW)). In addition, a duplicate set of samples were treated with a hydrophobing agent (water dispersion of siloxane and silicone resin).

The samples were stacked in front of a concrete masonry unit wall (9 cm), the rest of the wall area was covered with EPS insulation to keep the heat transfer uniform and as 1-dimensional as possible. The joints were tightened using elastomeric foam and mineral wool insulation.

Dantec ComfortSense 54T35 omnidirectional hot-wire anemometers were used to measure air velocity near the surfaces of all the samples. After iteratively tuning the speed of the fans recirculating the air inside the chamber and configuration of screen deflecting the air in front of the air inlets, the combination resulting in most uniform air velocity (v_{avg} = 0.31 m/s, SD=0.07 m/s) was chosen for the duration of the experiment.

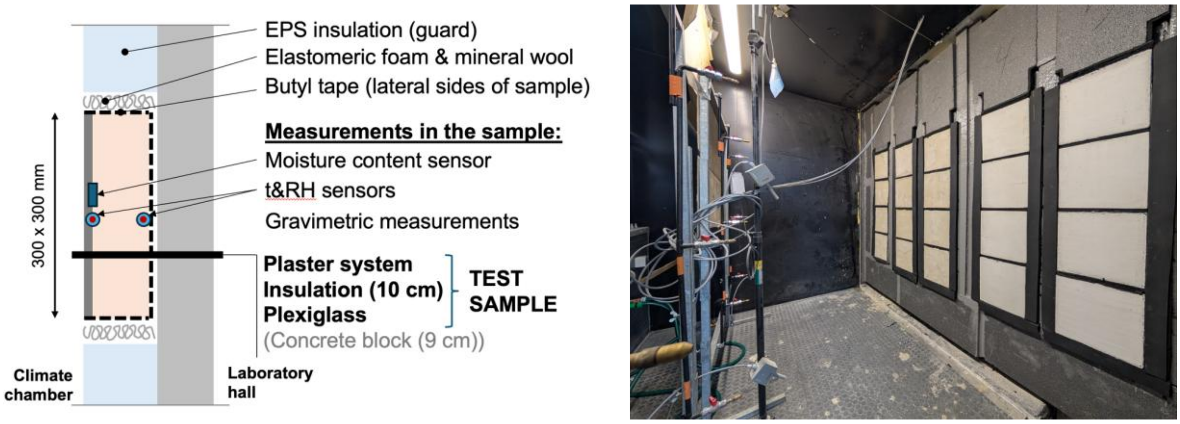

Figure 27. Schematic of the test sample (left) and samples installed in the climate chamber, spray nozzles for rain simulation are also visible (right). (Klõšeiko et al., 2026)

Table 5. Configurations of the tested samples (20 in total).

	Plaster system			
	THICK natural hydraulic lime		**THIN lime-cement**	
Total plaster thickness	ca 30 mm		ca 10 mm	ca 13 mm
Exterior surface treatment	Untreated OR hydrophobized		Untreated OR hydrophobized	
Finishing plaster	NHL finishing plaster		LC plaster, 3 mm	
	15 mm	20 mm		
Reinforcement plaster	NHL base plaster, 10 mm		Lime-cement plaster	
			3 + 4 mm	5 + 5 mm
Primer	LC plaster, 5 mm	-	-	
Insulation	**EPS, PF**	**MW, WFB**	**EPS, PF**	**MW, WFB**
Rear surface of the sample	Plexiglass 4mm OR concrete 30mm + PE tape		Plexiglass 4 mm	

3.2.2.2 Instrumentation

The samples were instrumented with capacitive Sensirion SHT35 temperature & humidity sensors both between the plaster and insulation (front side of the sample) and insulation and plexiglass (rear side of the sample). SHT35 sensors also measured the air temperature both inside the climate chamber and in laboratory hall behind the concrete masonry unit wall. Sensor data were collected using tailor-made dataloggers based on Arduino platform and stored on an SD-card and in Influx database at 10 second interval with real-time monitoring. All sensors were new, used for the first time and were factory calibrated. In addition, calibration was checked in the laboratory prior to the experiment in a constant temperature and humidity chamber. All sensors showed results similar to a reference sensor, temperature readings were in range of ±0.1 °C, humidity readings were within range of ±1% RH. No sensors were rejected, no additional correction factors on top of factory calibration were deemed necessary.

As the conditions at plaster and insulation intersection were predicted to be severe, the t&RH sensors there were also duplicated with Rotronic Hydroclip HC2-C05 sensors (logged using Grant Squirrel SQ2040-2F16) to serve as a reliable backup and comparison to the other more affordable sensors.

Due to diminishing accuracy of RH sensors at higher humidity ranges, Meter Group ECH2O EC-5 soil moisture sensors were installed in the plaster layer of some of the thick plaster samples to measure the moisture content throughout the experiment.

3.2.2.3 Test protocol

The testing program was designed to expose the plaster–insulation assemblies to controlled thermal, moisture and freeze–thaw loads representative of exterior wall retrofit conditions. After an initial dry-out and curing period to reduce built-in moisture, the samples were subjected to a sequence of thermal and moisture cycles with increasing severity. The test program consisted of the following steps:

1. Dryout of initial moisture, curing of plasters (ca 4 months).
2. Initial thermal cycling along with humidification in hygroscopic range.
3. Wetting (simulated wind driven rain for 4 h: constant water film sprayed on sample surfaces, water temp. ca 18.5 °C, air temp. ca 20 °C).
4. Drying, ca 1 month.
5. Wetting (partial immersion for 4 h, samples weighted throughout the immersion).
6. High temperature cycles (23 cycles; based on a measured summer situation, where plaster surface reaches ca 40 °C during the day due to solar radiation and ca 12 °C during night; air temp. in chamber: 5 hours at 10 °C, increase to 45 °C over 5 hours, 5 hours at 45 °C, decrease to 10 °C over 9 hours; air temperature in lab hall: 20 °C; see Figure 35 (left)).
7. Wetting (partial immersion for 4 h, to achieve initial humidity for freeze-thaw cycles)
8. Freeze-thaw cycling (18 cycles; air temp. in chamber: 7 hours at 10 °C, decrease to -20 °C over 6.5 hours, 10 hours at -20 °C, increase to 10 °C over 1.5 hours; air temp. in lab hall: 18–20 °C; see Figure 35 (right)).
9. Wetting (partial immersion for 9 h).
10. Freeze-thaw cycling (20 cycles).
11. End of climate chamber experiment; 15 x10 cm pieces were cut from the main samples and moisture content of plaster and insulation layers was measured gravimetrically.

3.3 Results and discussion

3.3.1 Freestanding outdoor test wall

For the time of writing this report, the test wall had been exposed to outdoor climatic conditions for nearly two years. However, the data analysis in this chapter was carried out over shorter time spans. The monitoring of temperature and RH inside the wall will continue in the future for long-term durability analysis.

3.3.1.1 RH measurements of facade plaster

Initial measurements from the 1st autumn, winter and spring, showed significant differences between plaster system types and insulation types. For the north-facing facade, thick plasters showed more stable RH than thin plasters for all insulation types. In thick plaster systems, RH exceeded 90% for over 90% of the time, while thin plasters exceeded 90% RH for about 85% of the time (Figure 28). However, thin plasters had considerably more hours at 100% RH, except on the PF-insulated section.

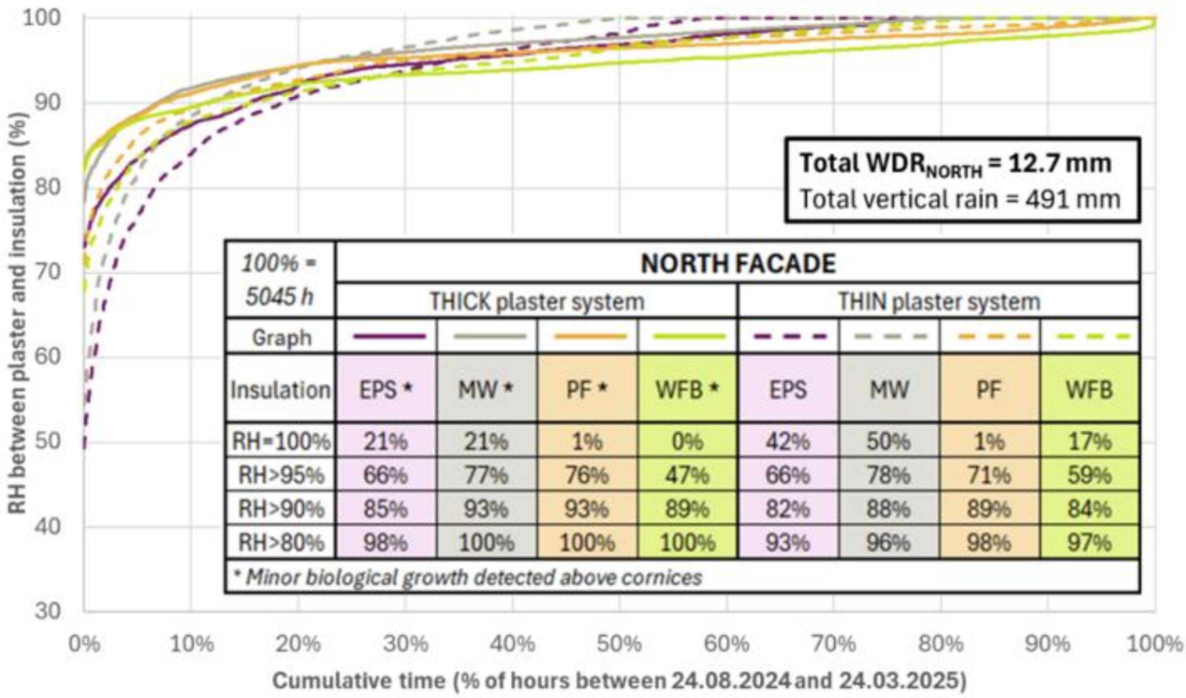

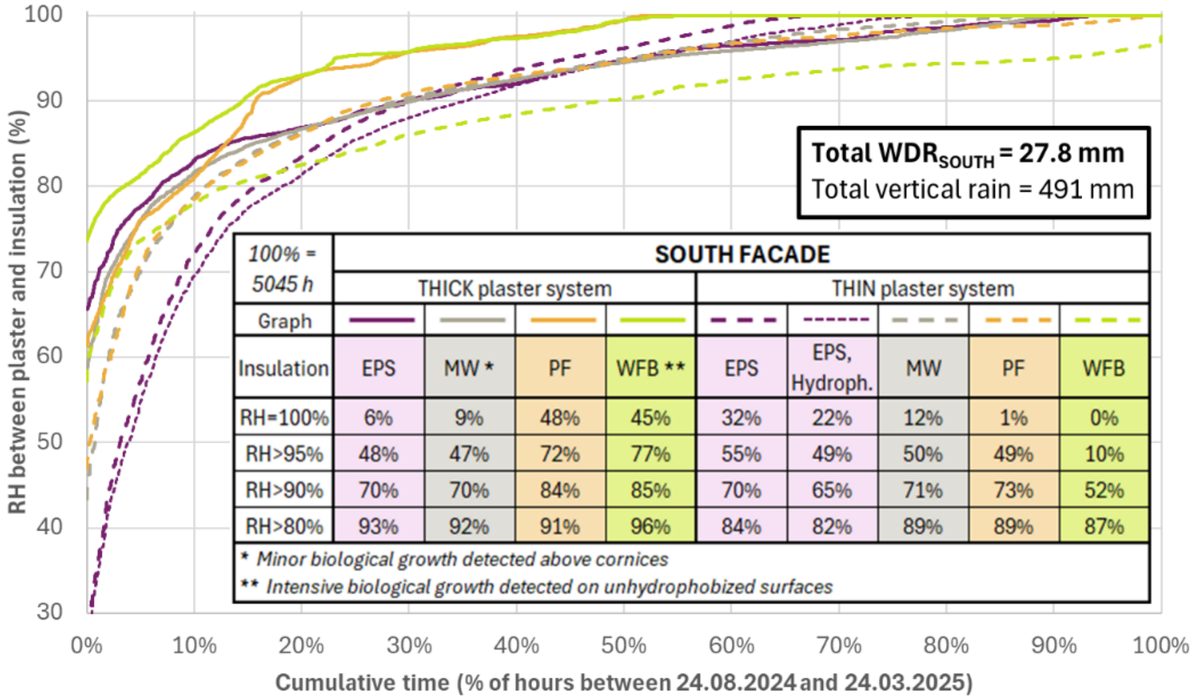

Figure 28: Cumulative hourly relative humidity between plaster and insulation layers for various insulation and plaster combinations on the north-facing facade (top) and south-facing facade (bottom). The percentages in the table indicate the proportion of time from 7-month period during which the corresponding RH threshold was exceeded. (Talvik et al., 2025)

To present the fundamental differences in the hygrothermal behaviour of thick and thin plasters, spring and autumn should be analysed separately. During the autumn period, the plasters become wetter over time due to increasing WDR load and reduced solar radiation on the surface. Therefore, in theory, a greater thickness and higher moisture buffering capacity of thick NHL plaster should keep the RH in the backer layers of the plaster system lower than in thinner L/C plaster systems. For the north orientation, this is confirmed by the measurements for all insulations: the 1 cm thick lime-cement plaster has more hours with RH < 97% than the thicker NHL plaster (Figure 29). On the south side, the situation is the same for EPS and MW insulation, but PF and WFB are drier in the case of 10 mm L/S plaster. Overall, the south façade had fewer hours with high RH than the north façade.

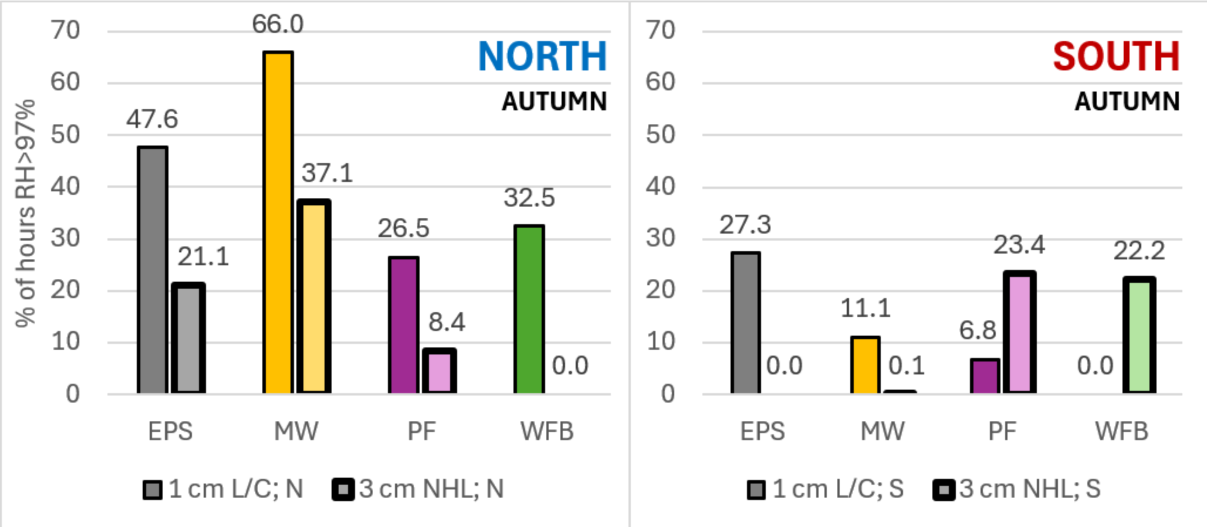

Figure 29: Proportion of hours at autumn (01.09. – 30.11.2024), when >97% RH was exceeded at the back side of the plaster system (Lemberg, 2026)

In spring, the effect of plaster thickness is also evident. A larger moisture mass dries more slowly, and this is especially visible on the south facade, where the thick NHL plasters remained at elevated RH levels for longer on every insulation combination tested (Figure 30). During winter, wind-driven rain and high outside RH increase the moisture content of the plasters, and in December and January, all the plasters are at or near 100% RH. Due to their higher moisture capacity, thick plasters are able to dry out less quickly in spring.

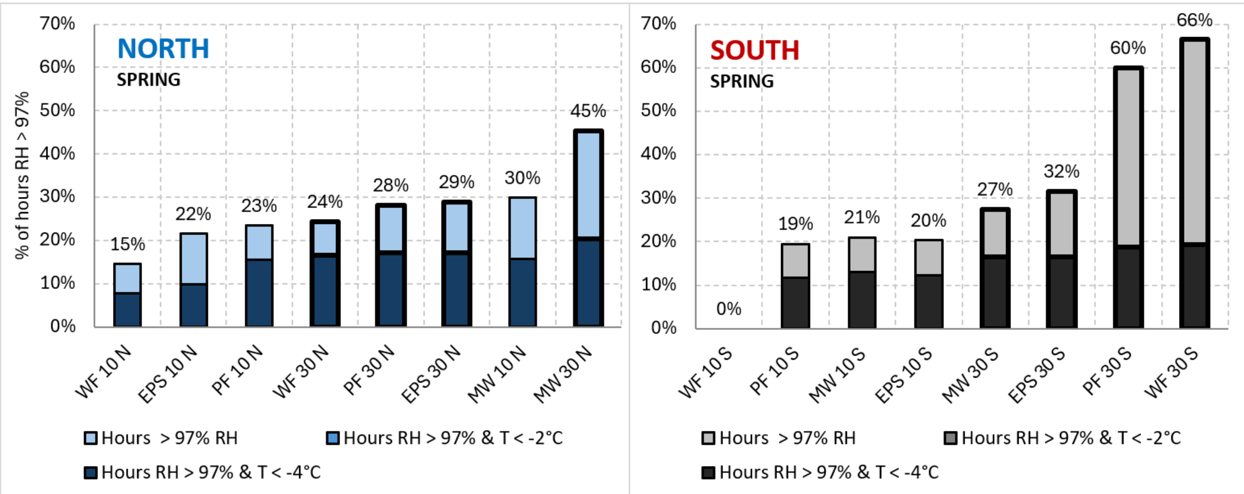

Figure 30: Proportion of hours at spring (01.02. – 23.04.2025), when >97% RH was exceeded at the back side of the plaster system. (Lemberg, 2026)

A slower drying process implies that thick plaster systems may be associated with a higher risk of mould growth, as elevated RH levels can coincide with temperatures that are already sufficiently high for mould growth. On the other hand, the more rapid changes in temperature and moisture content experienced by thinner plaster systems may lead to greater and faster deformations. Previous studies have noted that ETICS façade plaster systems in Estonia tend to crack in early spring (Olak, Talvik, et al., 2026; Talvik et al., 2023), when cold nights are followed by relatively warm days with clear skies and solar radiation reaches the façade surface at a low angle. In such conditions, a cold and moist plaster surface undergoes a rapid temperature increase and drying, while moisture-content gradients develop between the façade surface and the back surface of the plaster system. A larger moisture mass and more uniform cross-section of the thick plaster system could be beneficial in these situations, as the moisture-content gradient is distributed over a greater thickness, possibly reducing local gradients, however, this is something that would require further investigation.

3.3.1.2 Visual appearance

Until early December 2024, no biological growth was observed on any wall section. The first signs appeared on 23 January 2025 on the southern facade with thick plaster and WFB insulation, and the highest coverage was recorded on 25 March 2025 (Figure 31). Minor growth was also found on the southern mineral wool section with thick plaster and on all northern thick-plaster sections above the cornices. By April to June, growth was stable or declining, and by early August only a few colonies remained. No growth was observed on surfaces treated with a hydrophobing agent or on thin lime-cement plaster finished with silicate paint.

Figure 31: Biological growth on 25 March 2025 on the thick plaster (NHL system) on wood fibre board insulation all over the section on southern facade (left) and same area on 07 August 2025 (right). (Talvik et al., 2025)

The amount of mould growth on the surfaces was uneven. Around the cornices and the edges of the sections, visible areas of increased mould growth were observed. This was likely due to splash zones created by the WDR distribution and to shading from solar radiation for part of the day. For example, the ventilated façade had a 50 mm protrusion compared with the adjacent MW section with a thick NHL plaster system (Figure 32). In the shadow of this small corner, the mould growth was much more severe than on the rest of the surface. This may also occur on a real façade, where the geometry changes across the surface.

Figure 32: Biological growth observed on March 3, 2026, on a south-facing, thick NHL plaster over MW, adjacent to a thicker ventilated façade on the right. The figure presents the original photograph alongside an edited version, with mould colonies highlighted using Google Gemini 3.1 Pro.

Mould growth in the 2024/2025 winter was significantly more intense than in the 2025/2026 winter. The latter was much colder and drier than the 2024/2025 winter. This indicates that mould growth on these thick façade plasters is highly sensitive to outdoor conditions. In future climates, both WDR loads and outdoor RH are expected to be higher in Estonia and several other climates. Therefore, to reduce the risk of mould growth on façade surfaces, changing the paint type on NHL facades or applying hydrophobization should be recommended.

At the time of writing, the test wall had been exposed to outdoor conditions for two years. Therefore, final conclusions regarding cracking could not yet be drawn. In addition, the dimensions of the test wall are relatively small, and the resulting temperature and moisture deformations may therefore not fully represent the cracking that could occur on a real façade. Overall, no cracking was observed on the main façade surface. However, small cracks were observed on top of the cornices, appearing already during the second autumn (Figure 33).

The cornices on the test wall were intentionally built without additional protection in order to assess their durability. In practice, a cement-based liquid-applied waterproofing membrane and/or a steel sheet could be recommended for the top surface of the cornice. The cornices on the test wall were constructed with a >10° outward slope on the top surface, which should also be applied to real cornices, even when they are protected by waterproofing or a steel sheet.

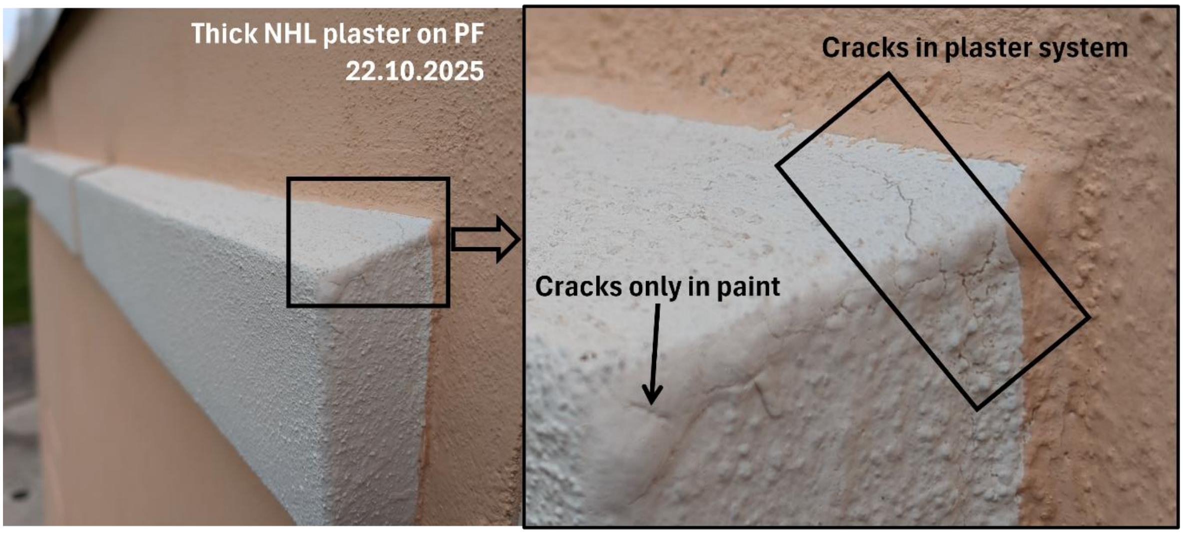

Figure 33: Small cracks observed at the corner of the cornice on 22 October 2025 on the south-facing façade with thick NHL plaster over PF insulation. The cracks may be the result of imperfect mesh installation around the cornice corners.

3.3.2 Climate chamber experiment

3.3.2.1 Overview of the experimental results

Figure 34 begins ca 4 months after the samples were produced and summarises the hygrothermal response of the plaster–insulation assemblies during the climate chamber phase of the experiment. The figures show temperature, relative humidity at the plaster–insulation interface and at the rear side of the insulation, as well as the gravimetrically determined moisture content. Relative humidity at the plaster–insulation interface and at the rear side of the insulation indicates that wetting is followed by internal moisture redistribution, which strongly influences the drying behaviour of the systems.

After wetting, mineral wool (MW) systems exhibited rapid vapour transport through the insulation, resulting in similar relative humidity levels at the plaster–insulation interface and at the rear side shortly after exposure. This indicates limited moisture storage and fast redistribution across the assembly, leading to comparatively uniform dry-out behaviour. EPS systems also reached high RH levels at both measurement locations, but with slower dynamics, indicating restricted vapour transport and prolonged moisture retention during dry-out.

Hygroscopic insulation materials showed a distinctly different response. In wood fibreboard (WFB) systems, relative humidity at the plaster–insulation interface remained high after wetting, while increases at the rear side were lower and delayed, indicating moisture buffering near the plaster layer. As drying progressed, buffered moisture gradually redistributed towards the rear side, which slowed down further dry-out of the system. Phenolic foam (PF) showed a similar but less pronounced behaviour, with short-term RH peaks near the plaster followed by partial initial drying and subsequently slower dry-out once moisture redistribution towards the rear side began.

Plaster thickness influenced both moisture storage and redistribution. The thick natural hydraulic lime (NHL) systems generally exhibited higher moisture levels and slower dry-out than the thin lime-cement (L/C) systems, particularly at the plaster–insulation interface. This suggests that the larger moisture capacity and higher thermal inertia of the thick plaster layers prolong the redistribution phase following wetting, whereas thinner plaster systems tend to dry more directly once external moisture supply is removed.

Overall, the comparison between the plaster–insulation interface and rear-side measurements demonstrates that drying of the tested systems after wetting is governed by internal moisture storage and redistribution mechanisms, which depend on both insulation material and plaster thickness.

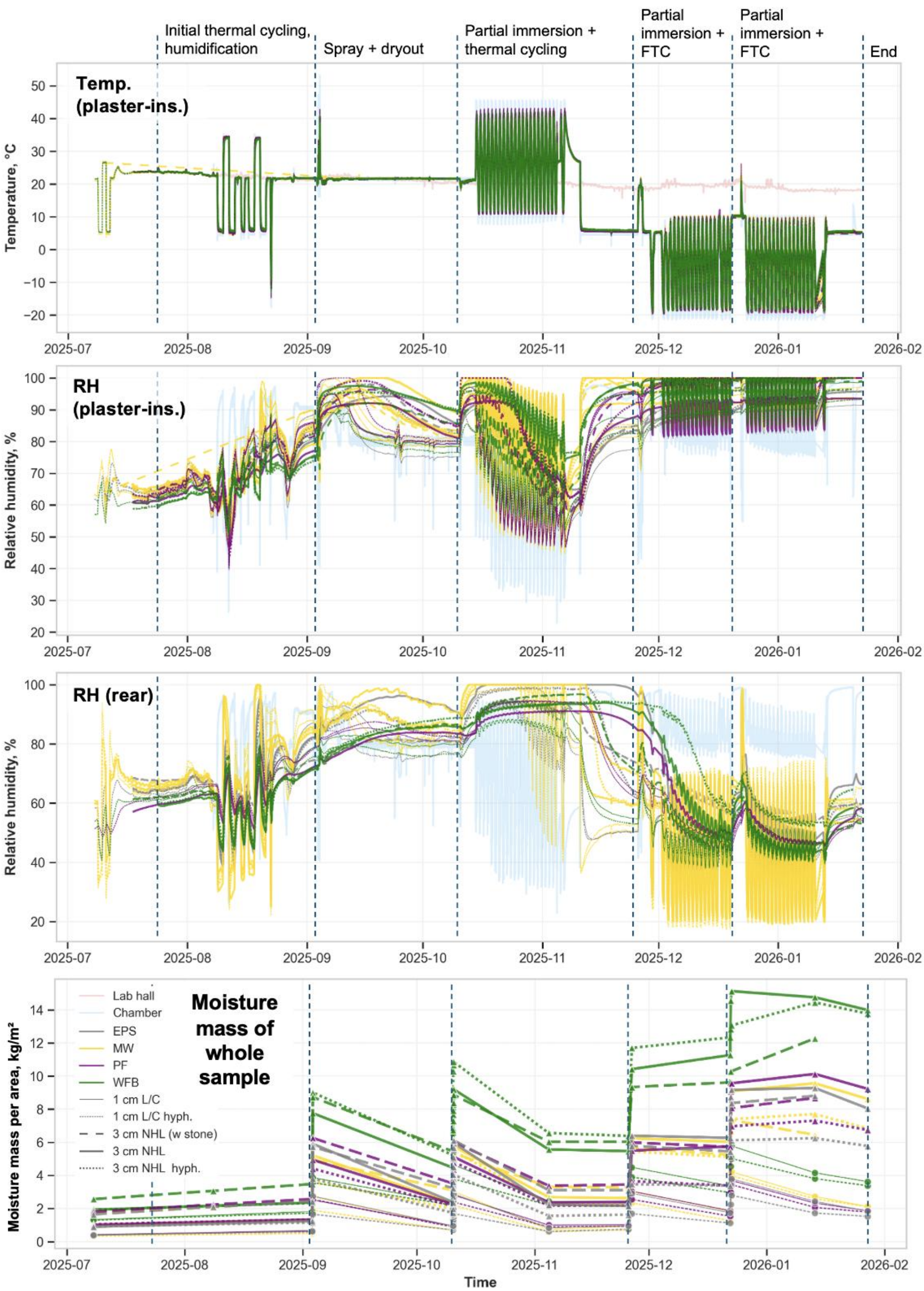

Figure 34. Measured temperature, relative humidity and moisture mass throughout the climate chamber phase of the experiment. (Klõšeiko et al., 2026)

3.3.2.2 Thermal and freeze-thaw cycling

Figure 35 (left) gives the temperature and humidity conditions in the samples during **thermal cycling** after the second wetting period and mimics the situation where solar radiation heats the plaster layer during summer. As the thick plaster system (especially in combination with wood fiberboard insulation) had higher thermal mass, the temperature behind the plaster layer stays lower than in samples covered with thin insulation. Effects of vapour permeability and hygroscopicity are also visible: as the temperature in moist plaster layer increases, the moisture flux is directed towards the rear of the samples and differences can be seen in the dynamics of relative humidity levels in front and behind the insulation.

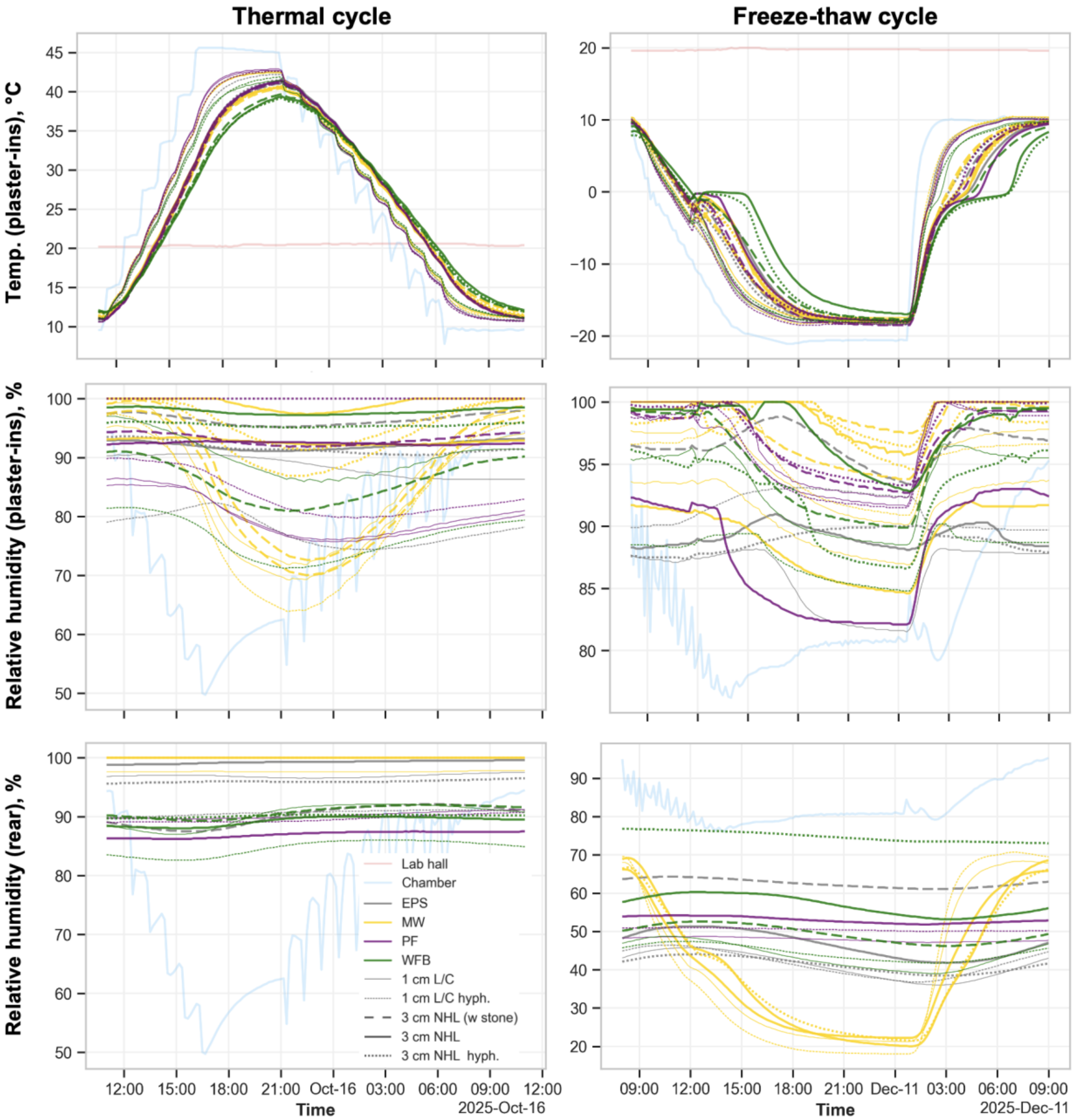

Figure 35. Left: thermal cycle mimicking hot summer day and causing moisture flux towards rear side of the sample. Right: a freeze-thaw cycle that spans 25 hours. Top row: temperature at plaster-insulation interface, middle row: relative humidity at plaster-insulation interface, bottom row: relative humidity at the rear side of the samples between insulation and plexiglass/concrete slab. (Klõšeiko et al., 2026)

While both MW and WFB are vapour open, WFB is hygroscopic and buffers the humidity fluctuations, at the same time MW section shows ca 30%$_{RH}$ fluctuations on the exterior side and nearly constant 100%$_{RH}$ levels at the rear side of the insulation. Condensation was also visible between plexiglass and insulation after thermal cycling on virtually every sample.

An example of a **freeze-thaw cycle** is given in Figure 35 (right). The latent heat of freezing and thawing can be seen, especially on thick plaster systems where the moisture mass is higher. Humidity fluctuations showed similar patterns as during thermal cycles, however, the vapour flux was mainly directed towards the exterior side due to reversed boundary conditions. No visible damage was detected due to the cycling at any stage of the experiment.

3.3.2.3 Wetting

The first wetting phase was conducted using spray nozzles covering the surface of the samples in the wall of the climate chamber with a constant water layer for 4 hours. After ca 1 month of drying at 20 °C and 80 %$_{RH}$, the samples were wetted again through partial immersion for the same duration as before. Figure 36 gives the results from these 2 tests: although the method and orientation were different, the LC plasters achieved almost identical mass increase both times and between insulation materials. Curiously, the 3 cm NHL + WFB samples absorbed more moisture than the others. As the mass increase was followed throughout the second wetting event (Figure 37), causes of the differences can be discussed: due to steady mass increase, the moisture front is probably still within the plaster layer and the insulation material does not affect the process and the possible reason is the unevenness of the NHL plaster layer itself (e.g. some cracking took place on top of the sensor cables). The hydrophobized samples absorb less water during the first weighting interval than the untreated samples, but the treatment seems to have little effect in later stages. Similarly, in an experiment by Slapø et al. (Slapø et al., 2017) on masonry various hydrophobing agents failed to prevent water ingress at areas where contact between mortar and bricks was not perfect.

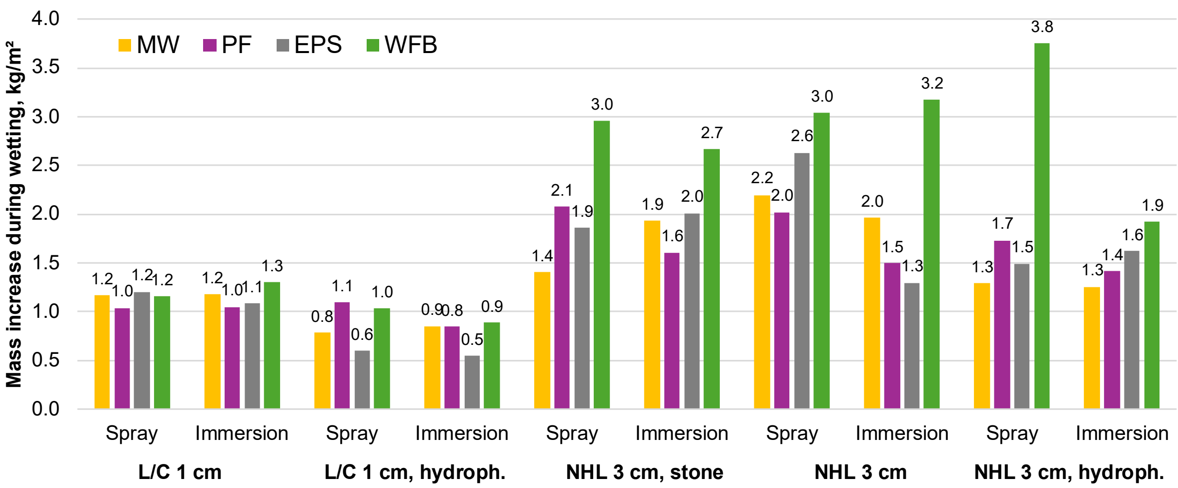

Figure 36. Comparison of mass increase during wetting through simulated rain ("spray") and partial immersion before freeze-thaw cycling (duration of both: 4h). (Klõšeiko et al., 2026)

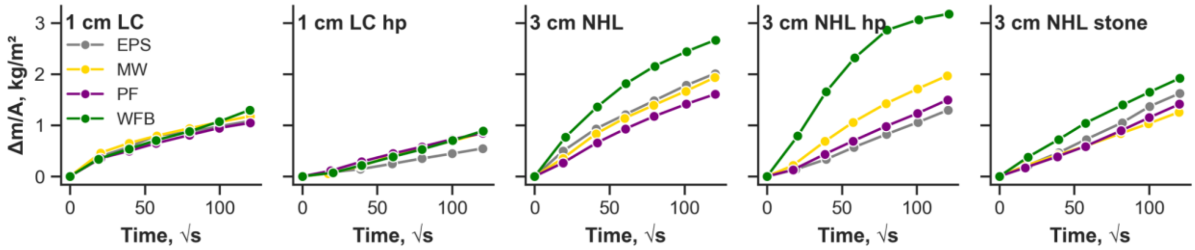

Figure 37. Mass increase during the second water exposure event (partial immersion), before FTC. (Klõšeiko et al., 2026)

At the end of the main experiment, the samples were cut to determine the **moisture content of plaster and insulation layers at the end of the experiment** (Figure 38) gravimetrically. There is a clear distinction between hygroscopic insulation materials (WFB and to some degree PF) and non-hygroscopic ones with WFB having an order of magnitude higher moisture content than EPS or MW. However, the 1 cm LC plaster layers of WFB and PF samples exhibited lower moisture content than those on EPS or MW. Hydrophobized 3 cm NHL samples had significantly lower moisture content of the plaster layer than untreated ones except for hydrophobized 3 cm NHL on WFB, which resulted in highest moisture contents in both plaster and insulation.

An important observation is the opposite behaviour of 1 cm LC and 3 cm NHL systems during FTCs – throughout this phase moisture content (Figure 34, bottom) of the LC plasters decreased, while the higher thermal mass of the thick plasters resulted in condensation/rime ice forming on their surface during the melting periods of the FTC-s. This could also explain the higher moisture content of the NHL samples at the end of the study.

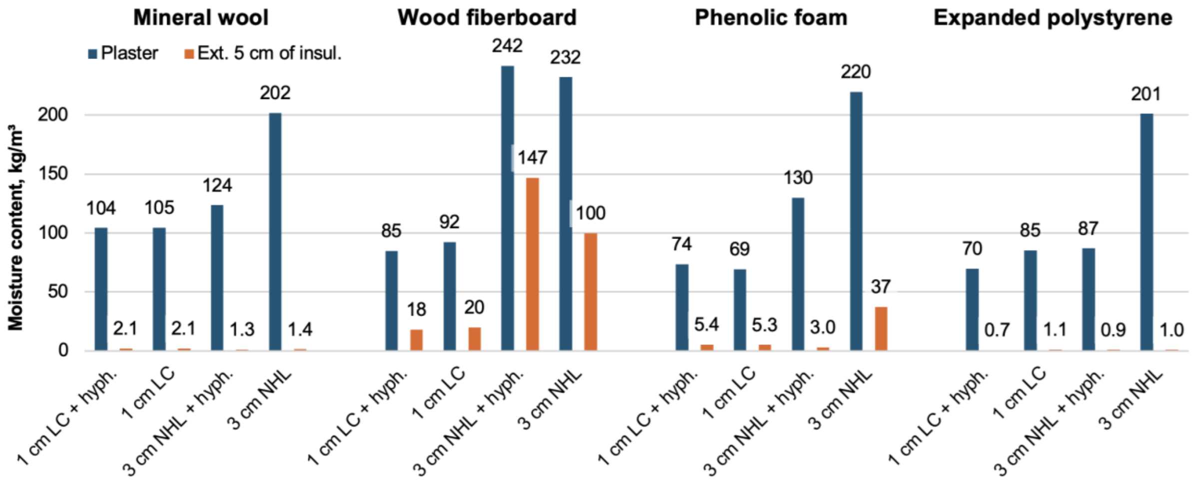

Figure 38. Moisture content of plaster and exterior 5 cm of insulation layers at the end of the experiment. (Klõšeiko et al., 2026)

4. Hygrothermal modelling

4.1 Introduction

The boundary conditions at the test wall locations are relatively mild; the site experiences only moderate wind speeds and WDR loads, and the climate during the measurement period is unlikely to be extreme. Furthermore, the limited height of the wall reduces the severity of these conditions. Likewise, the boundary conditions in the climate chamber are not directly comparable to long-term exposure under real climatic conditions.

Therefore, these experiments were used as comparative measurement data to ensure that the model satisfactorily reproduced the measured behaviour of the plaster systems. Using the model and knowing the performance limit, the performance of the façade system can be simulated in different climates, over extended periods of time, and for different building heights and geometries. Consequently, hygrothermal modelling is a critical part of this product development process.

4.2 Methods

4.2.1 Modelling tool

Delphin 6.1 software (Grunewald, 1997; Nicolai et al., 2009) was used for HAM modelling. Delphin uses the implementation of the ice model by Nicolai and Sontag (2013) to take the phase change enthalpies and freezing point depression (model by Häupl and Xu (2001)) into account.

4.2.2 Model setup

Modelling was carried out using 1D models. Their schematic representation is given in Figure 39.

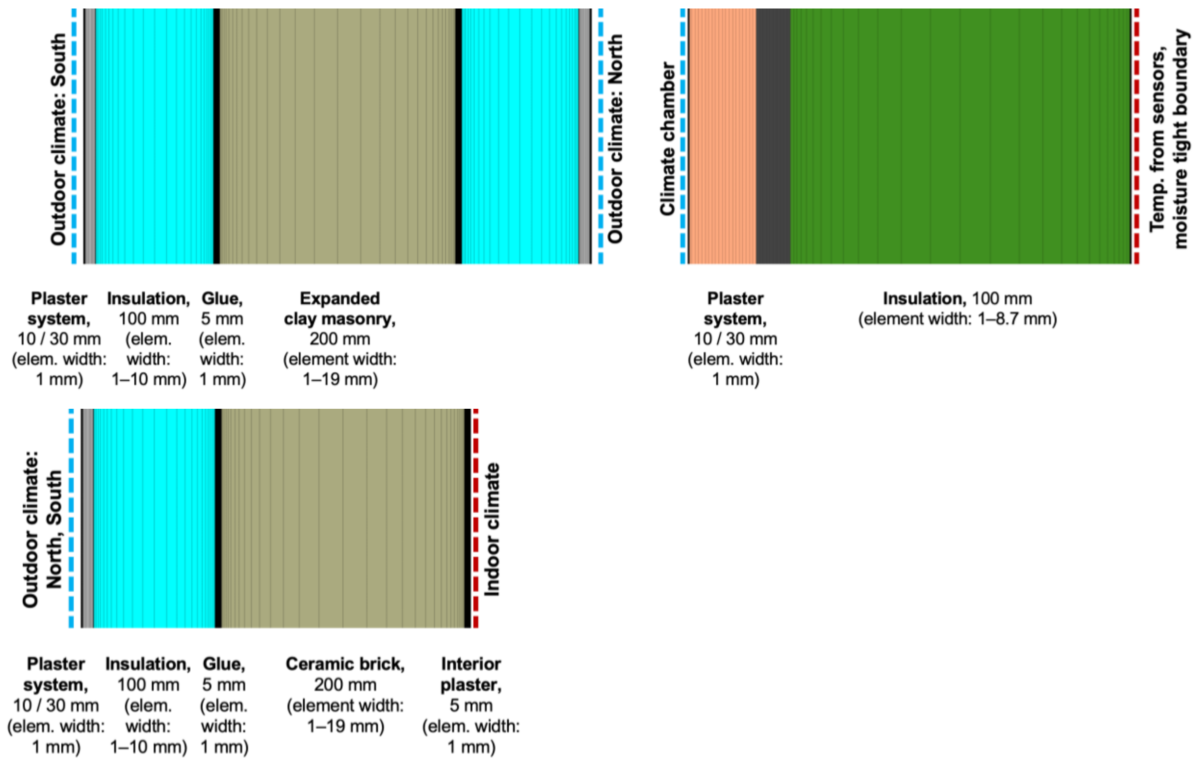

Figure 39: Schematics of the hygrothermal models: outdoor test wall (top left), climate chamber experiment (top right) and exterior wall in moisture reference year (bottom left).

4.2.3 Material properties

Table 6 gives the overview of the basic properties of materials used in modelling. The material files for ETICS plasters were based on measurements and they are further described in section 2.3.1.1.

Table 6: Basic material properties used in hygrothermal models.

Material	ID in Delphin database	Density ρ, kg/m³	Thermal conductivity λ, W/(m·K)	Spec. heat cap. c, J/(kg·K)	Wat. vap. diff. resistance coeff. μ, -	Porosity ψsat, m³/m³
Plasters						
Plaster NHL-1	-	1 590	0.662	757	12.2	0.374
Plaster NHL-2	-	1 510	0.858	880	18.9	0.39
Plaster KAM-R	-	1 510	0.962	733	15.6	0.395
Interior plaster	1828	1 647	0.67	990	3.4	0.189
Insulation materials						
Mineral wool	-	67	0.035	840	1	0.9
EPS 60 Silver	-	14	0.031	1 350	30	0.935
Wood fiberboard	693	160.8	0.039	1 662	3.45	0.55
Phenolic foam	689	35.5	0.02	1 470	114	0.501
Masonry						
Ceramic brick	496	1 851	0.659	794	12	0.283
Expanded clay block	-	740	0.2	894	8.82	0.65
Glue for insulation	-	1 164	0.289	1 461	13.1	0.38

4.2.4 Boundary conditions

Table 7 describes the boundary conditions assigned to the different models. For model calibration of the test wall, on-site measured climatic data were used as boundary conditions. For model calibration in the climate chamber, measured boundary conditions from the chamber tests were used. This allowed the model to mimic the hygrothermal behaviour of the real test wall, and the measured data from the both experimental setups could be compared to the modelled outputs.

As the wall setup is sensitive to WDR loads, special attention was paid to accurately model the WDR load. In addition to using different measurement devices for wind and rain data (Figure 25), a CFD model was created for the test wall location (Figure 26).

Table 7: Overview of boundary conditions used at different stages of modelling.

		Left boundary	Right boundary
Comparison of modelling and measurement results	**Outdoor test wall**	Measured outdoor climate parameters on the South side wall	Measured outdoor climate parameters on the North side of the wall
	Climate chamber experiment	Temperature & relative humidity measured in climate chamber	Temperature measured on the rear side of every sample, no moisture transfer
Modelling with moisture reference years (MRY)		Outdoor climate: Estonian Moisture Reference Years (Kalamees & Vinha, 2004) for: • condensation assessment • mould risk assessment	Indoor climate: • indoor temperature model based on the indoor climate of Estonian brick apartments corresponding to the lower limit of Fig. 7 in Ilomets et al. (2018). • Indoor humidity load based on moisture class 3 from Estonian National Annex to EVS-EN 15026:2023/NA:2025, Figure NA.2

4.2.5 Performance criteria

4.2.5.1 Frost damage

According to study by Feng et al. (2019) the onset of frost damage requires a certain degree of saturation along with temperature low enough. As determined in section 2, the significant change in ultrasonic pulse velocity (i.e. frost damage) was detected at 100%$_{sat}$, while at 70%$_{sat}$ there was no change yet. In order to stay conservative and until the exact threshold of damage is further measured, the 70%$_{sat}$ is used as performance limit.

4.2.5.2 Finnish mould growth model

Several models for mould growth assessment exist. Within the scope of this study, the Finnish / VTT mould model (Hukka & Viitanen, 1999; Ojanen et al., 2010; Viitanen et al., 2011) is used due to its versatility and applicability to both measurement and modelling results. The model offers two methods to assess the situation – the critical relative humidity above which mould growth is possible and mould index. The former depends on material sensitivity and temperature (see Figure 40, left), the latter considers the material characteristics, temperature, relative humidity and the duration of conditions favourable for mould growth and returns the mould index value from 0 (no growth) to 6 (extensive mould growth) – see Figure 40, right.

According to Viitanen et al. (2015) the unacceptable mould index for interfaces and surfaces which are not in direct contact with the interior air is > 3 while values between 2–3 should be treated with caution.

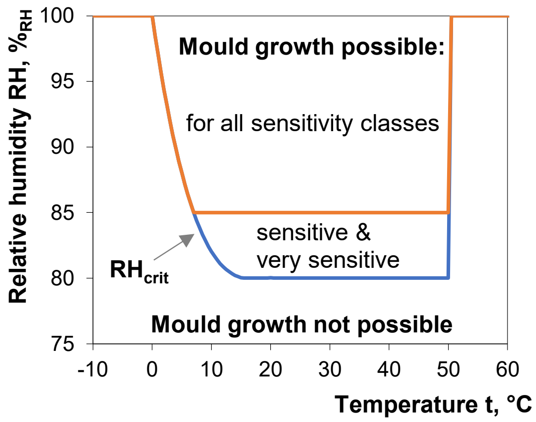

Mould index	Growth rate
0	No growth
1	Small amounts (microscope)
2	Several colonies (microscope)
3	Visual findings (< 10% coverage) or < 50% coverage (microscope)
4	Visual findings (10–50% coverage) or > 50% coverage (microscope)
5	Plenty of growth (> 50% visual coverage)
6	Heavy and tight growth (≈ 100% visual coverage)

Figure 40: Left: critical relative humidity (RH_{crit}) above which mould growth is possible according to the Finnish mould model. Based on Viitanen et al. (2011). Right: mould indexes along with corresponding descriptions of growth rate and colors denoting acceptability on surfaces in contact with interior air (green – acceptable; yellow – warning; red – unacceptable). Based on Viitanen et al. (2015).

4.3 Results and discussion

4.3.1 Comparison between measurement and modelling results

4.3.1.1 Initial Modelling of the Outdoor Test Wall with Different WDR Load Input Methods

Initial modelling of the test wall showed that the model is highly sensitive to WDR load. This was also expected by design, as one of the core principles of the insulated façade system is the use of thick façade plaster layers. Therefore, considerable effort was devoted to understanding how different WDR loads affect the moisture behaviour.

Different approaches for determining WDR loads were compared using data from a local weather station, nearby meteorological stations, and direct WDR measurements carried out on-site. In addition, CFD modelling was used to estimate the difference between the WDR load measured by the collection screens and the actual load reaching the façade surface (Talvik et al., 2026).

The directly measured WDR load was generally higher than the WDR loads calculated from nearby meteorological stations according to EN ISO 15927-3. Data from the on-site conventional weather station showed the closest agreement with the measured WDR loads and, in the case of the northern façade, even slightly higher values.

A comparison between directly measured and calculated WDR rates showed that the direct measurement devices systematically missed very small rain events. This was caused by the inertia of the measuring system, as the collection screen and tubing had to become wet before water reached the tipping-bucket mechanism. As a result, the calculated WDR datasets contained a large number of small rain events that were not detected by the direct measurement devices.

CFD simulations indicated that the collection screens received slightly higher WDR loads than the monitored façade surface. Based on the CFD results, a correction coefficient of 0.8 was applied to convert measured WDR loads from the collection screens to the actual façade surface. When these CFD-corrected WDR loads were used in DELPHIN simulations, the agreement between measured and simulated relative humidity improved compared to simulations using the raw direct WDR measurements.

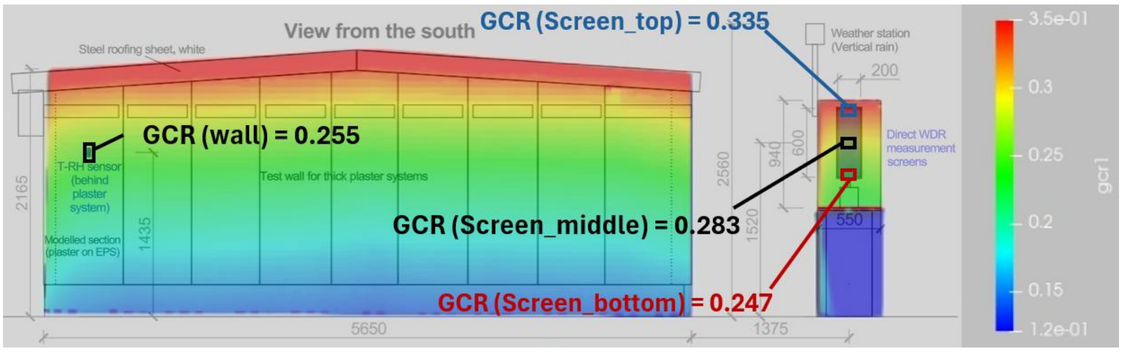

Figure 41: Global catch ratio (GCR) distribution of WDR on the southern facade and WDR screen in case of wind direction 255°, wind velocity 2 m/s (h=2.5 m) and vertical rain rate of 1.0 mm/h. (Talvik et al., 2026)

The hygrothermal simulations showed that the choice of WDR input has a significant influence on the predicted moisture conditions behind the façade plaster system. Based on the comparison with measured RH, the most accurate results were obtained using local weather station data together with the EN ISO 15927-3 calculation procedure and using CFD-corrected direct WDR measurements. Therefore, these two approaches were considered the most suitable for further hygrothermal analysis of the test wall, and local climate monitoring is recommended for similar experiments in the future.

The statistical comparison showed the closest agreement between measured and modelled RH using the on-site conventional weather station data, which slightly underestimated RH (MBE = -1.9%; RMSE = ±15.6%). Direct WDR measurements with a CFD coefficient also performed well, giving a conservative overestimation of 3.3%. For future modelling, combining these two datasets is recommended.

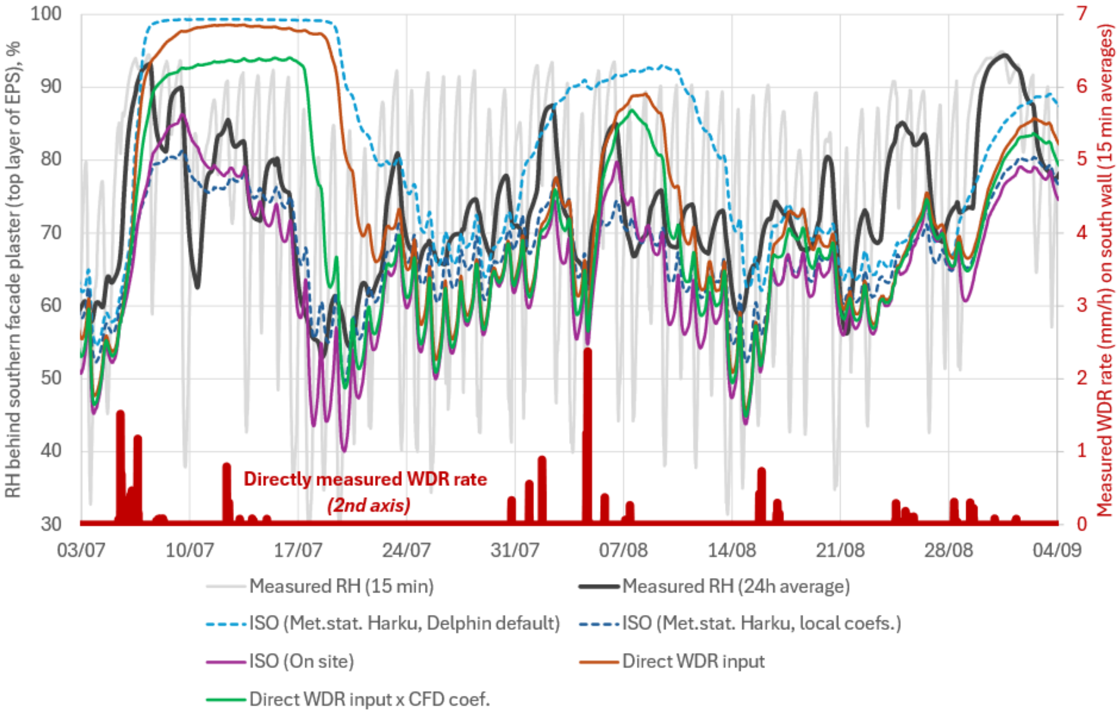

Figure 42: Measured and simulated RH behind a 10 mm thick plaster on EPS at the south-facing facade under varying WDR load assumptions. (Talvik et al., 2026)

4.3.1.1 Model assessment based on climate chamber experiment

The modelled relative humidity (Figure 43) and moisture content (Figure 44) of plaster layer were compared to measurement results. Both modelled RH and moisture content in the plaster layer are overestimated compared to measurement results. While the overall trends match, the main discrepancies arise during the wetting episodes, where the modelled amount of absorbed water is exaggerated and also causes prolonged dryout.

This is probably due to different behaviour of small-scale material characterization NHL plaster samples used in water uptake experiments compared to the samples used in climate chamber study. The small-scale samples were 50x50x50mm cubes which were cast as a monolithic block, while the plaster of climate chamber experiment was both thinner (prescribed layer thicknesses) and applied in layers over several days, representing a more realistic scenario. The water uptake coefficient measured from small scale samples is 3-5x higher compared to analogous experiment in climate chamber – as the transfer functions for modelling were fitted according to the results from small-scale samples, the modelling does not yield results comparable to the climate chamber measurements.

However, the water uptake coefficient of 50x50x50mm cube NHL samples was similar to the samples where frost damage was indicated using ultrasonic pulse velocity measurements and a sudden increase in water uptake rate was also detected. Hence, the modelling results could be considered indicative of the performance of a frost-damaged plaster.

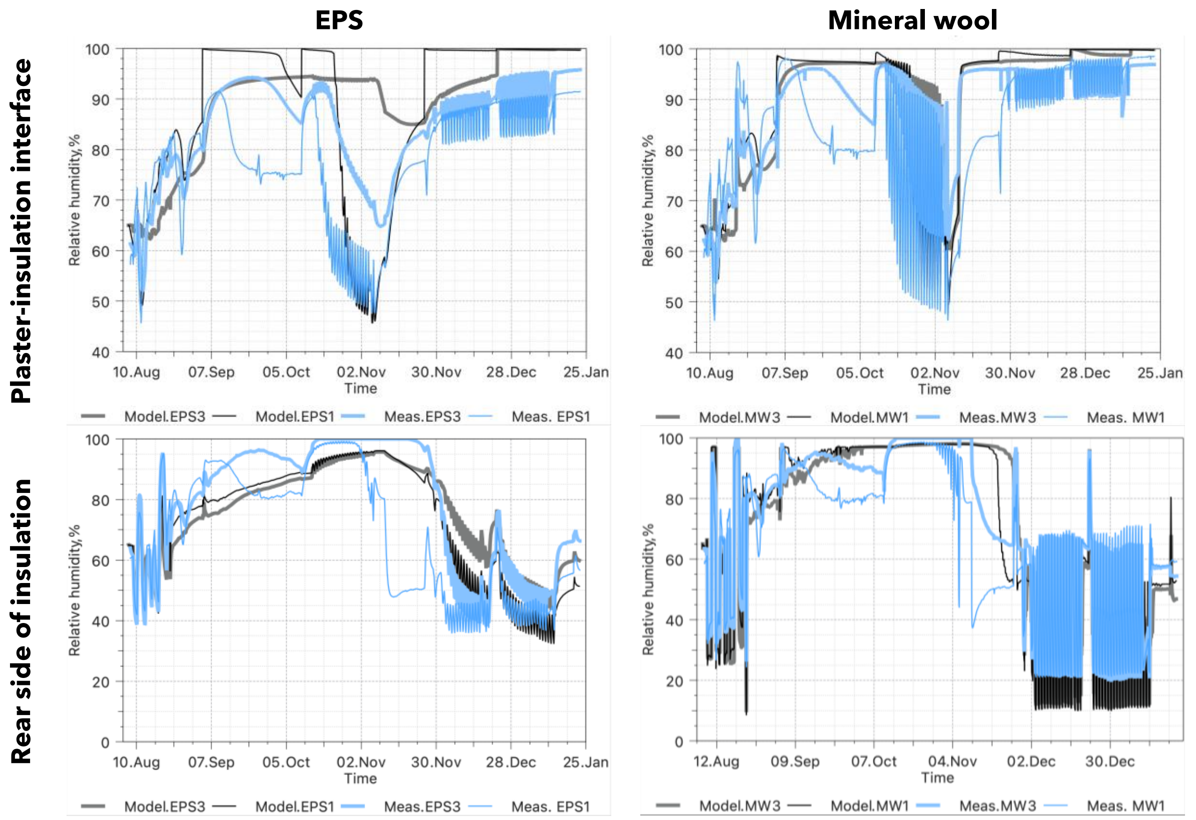

Figure 43: Comparison between measured (blue lines) and modelled (black lines) relative humidity in 3 cm NHL (thick lines) and 1 cm LC (thin lines) plaster systems.

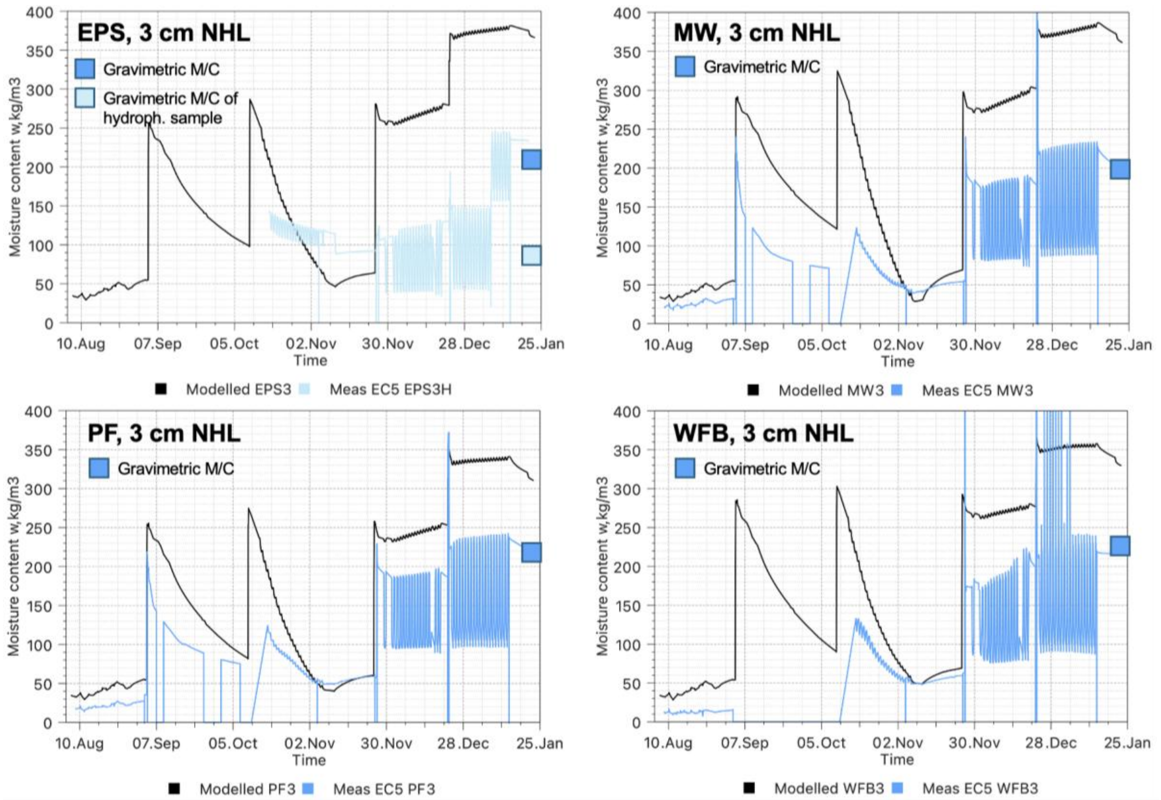

Figure 44: Comparison between measured (blue lines) and modelled (black lines) moisture content in 3 cm NHL plaster samples. Squares denote the gravimetrically determined moisture content at the end of the experiment. Note: untreated EPS did not have an EC5 moisture content sensor, measurements from hydrophobized sample are used.

4.3.2 Modelling with moisture reference years (MRYs)

4.3.2.1 Mould risk

Mould risk assessment MRY was more critical for mould growth assessment as the mean temperature is higher than that of the condensation risk MRY. Based on their origin, most of the materials (e.g. plasters, EPS, MW, PF) used in the study belong to mold sensitivity class MSC3 ("medium resistant"). The exception is WFB which according to its bio-based origin could belong to MSC2 ("sensitive", which applies to e.g. spruce and treated wood fibre boards). This is tentative, as the mould sensitivity class have not been determined experimentally here.

The only significant increased mould index took place inside the ETICS (between plaster and insulation) when WFB was used as insulation (see Figure 45). On the exterior surface and in other combinations of insulations and plasters the modelling did not indicate a mould risk above MI 1 ("Initial stages of growth").

It was found that in the event of high rainfall loads, there is no difference between the 30 mm and 10 mm plaster solutions. For both plaster thicknesses, the mold index on the south-facing wall exceeded 5—meaning that the model predicts visible mold growth on at least 50% of the surface. On the north-facing wall, where the amount of water falling on the wall is more than three times lower, a difference emerges between the 10 mm and 30 mm plaster solutions. In this case, only the 30 mm plaster variant exceeds a mold index of 3, meaning the model predicts visible mold growth on up to 10% of the surface.

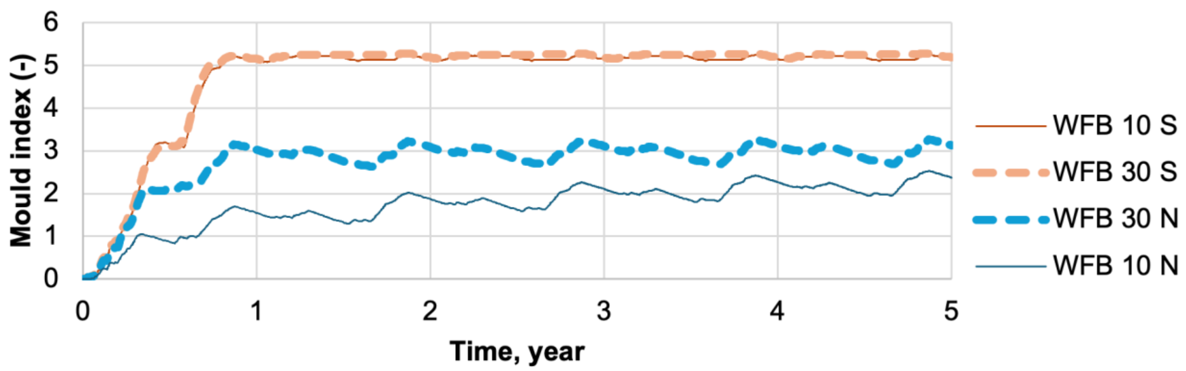

Figure 45: Modelled mould index between plaster and wood fiberboard insulation, Estonian mould risk MRY.

Some aspects that should be kept in mind:

- The VTT mold index was originally developed to assess mold growth on surfaces exposed to air, rather than within the material itself.
- Material properties used for modelling probably overestimate the amount of absorbed water in the plaster layer, resulting in high moisture content in the plaster and WFB layer.

Previous studies have identified mould growth on paraffin-treated WFB roughly equivalent to mould index 3-4 after 60 days above water bath at 23 °C, while moisture content of the WFB was 2.1 kg/kg ≈ 230 kg/m³ (Imken et al., 2020).

4.3.2.2 Evaluating frost damage risks based on hygrothermal modelling

The results from 5th year of condensation risk MRY models show that the differences between orientations were greater than the differences between plaster systems/thicknesses (Figure 46). The north-facing façade, which received less WDR due to the prevailing south-west winds, showed much lower ice saturation degrees and the tentative 70%$_{sat}$ frost damage threshold was not exceeded.

On the south facade the 30 mm thick façade plaster performed worse than the thinner 10 mm lime-cement plaster system in the case of EPS and MW insulation. The façade with PF insulation showed fewer freeze-thaw cycles overall, and in case of PF the thick 30 mm plaster performed slightly better than the 10 mm lime-cement plaster.

Again, it is necessary to state that the material properties are probably overestimating the amount of absorbed rainwater in the plaster layer, resulting in high moisture content in the plaster and WFB layer.

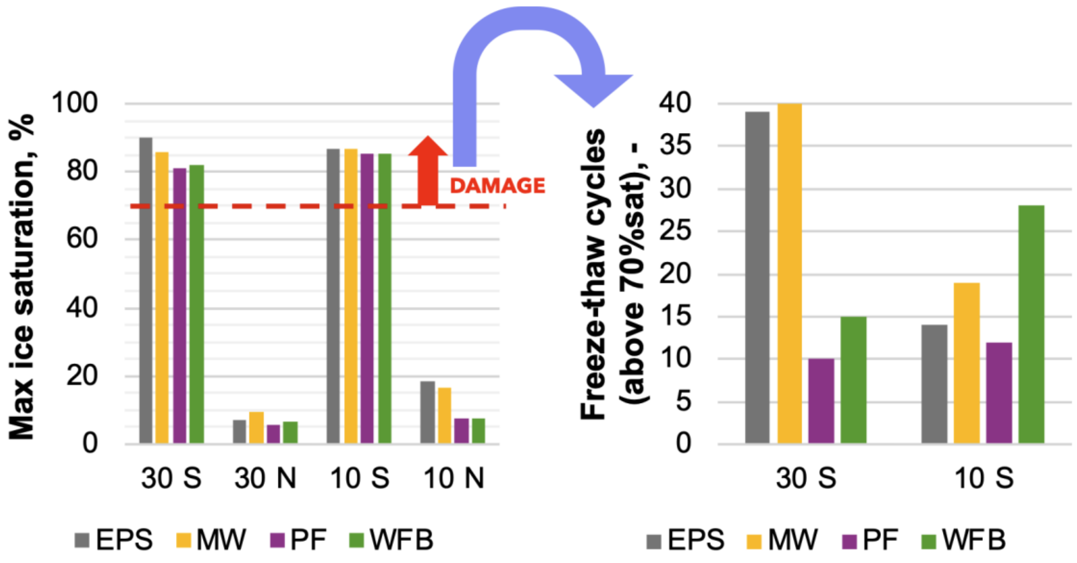

Figure 46: Modelled maximum ice saturation degrees with the test wall climate and freeze-thaw cycles for combinations where 70%$_{sat}$ was exceeded. (Lemberg, 2026)

5. Conclusion

5.1 Findings from specific investigations

5.1.1 Material level studies

Hygrothermal characteristics of the plasters were determined and primary hygrothermal material models were established for all investigated plasters based on experimentally determined moisture storage, vapour transport and liquid transport properties.

Despite exhibiting similar density, open porosity and capillary saturation moisture contents, the investigated plasters showed differences in moisture retention behaviour from the onset of the overhygroscopic moisture range up to capillary saturation, with NHL-2 retaining substantially less moisture than NHL-1 and KAM-R at a given suction pressure.

Capillary water absorption coefficients were found to be strongly dependent on specimen geometry, manufacturing method and boundary conditions. Substantially different A_w values were obtained for the same plaster materials when measured on the 20 mm thick plaster layers used in the frost resistance investigation and on the 50 × 50 × 50 mm cast specimens used for material characterization. While the measured A_w of KAM-R was only marginally higher for the cast cubic specimens, the corresponding values for NHL-1 and NHL-2 increased by approximately 8 and 7 times, respectively. These results indicate that capillary water uptake measurements of NHL-based plasters are particularly sensitive to specimen preparation and test configuration, whereas the measured water absorption behaviour of the lime-cement plaster KAM-R was comparatively less affected.

Wood fibre board exhibited pronounced thermal anisotropy, with thermal conductivity measured parallel to the board plane approximately 50% higher than that measured through the board thickness, highlighting the importance of accounting for material orientation in hygrothermal simulations.

Phenolic foam exhibited a strong humidity dependence of vapour transport properties, with the vapour diffusion resistance factor decreasing from approximately 80 under dry-cup conditions to below 3 under wet-cup conditions, indicating a substantial increase in vapour permeability at high relative humidity.

Onset of frost damage in all tested plasters takes place between 70–100%$_{sat}$ (tested at -20°C), while the testing showed correlation between the onset of frost damage and 3-5x increase in water uptake coefficient.

5.1.2 Outdoor test wall

The outdoor test wall proved to be a very useful installation for studying the construction technology of different fixings, reinforcements, plastering methods, and the formation of cornices and grooves. It also provided an early insight into the durability and mould-growth resistance of different plasters and paints. The main benefit was the long-term temperature and relative humidity measurement data inside the wall as well as measured local climate data, which are in combination useful for model validation and important stepping stone for hygrothermal modelling in other climates. Furthermore, the test wall is a valuable tool for demonstrating different stakeholders (municipal authorities, homeowners, researchers) the actual look, feel & possibilities of the proposed systems and has resulted in positive feedback from them.

5.1.3 Climate chamber study

The thick NHL plaster system generally exhibited higher moisture content values compared to thin LC plasters due to their higher water absorption coefficients. However, while the 4–9-hour wetting through constant water contact is suitable for hygrothermal model calibration, it might not be very representative of hygric loads facing the real wall assemblies. Furthermore, the redistribution of moisture from 1 cm LC to 3 cm NHL samples during melting periods through evaporation and condensation/freezing on NHL samples (with higher thermal mass) is also a product of the closed system of the climate chamber and accelerated thawing process, not necessarily actual service conditions. Therefore, suitability assessment will be based on results of hygrothermal modelling and measurements from the outdoor test wall.

The hygric buffering effects of WFB and to some degree of PF were evident, possibly providing the tools to smooth out the extreme saturation degrees in the plaster layer to avoid frost damage.

The currently used hydrophobing agent exhibited limited effect when exposed to prolonged water contact (mainly detectable during the very initial stages of exposure). This was possibly due to very limited penetration of the agent into the plaster. However, moisture content of hydrophobized 3 cm NHL plaster samples was 1.5–2x lower than that of the untreated counterparts.

5.1.4 Hygrothermal modelling

Comparison between measured and simulated values revealed that modelling with current material properties overestimated the amount of absorbed water both due to spray and water contact in climate chamber experiment. This resulted in ca 1.5-2x higher moisture content than measured at the end of the modelling period, which suggests that the modelling results could be conservative.

Modelling with Estonian moisture reference years (MRY) shows that results depend heavily on wind-driven rain (WDR) loads. While high WDR (South) causes both 1 cm LC and 3 cm NHL systems to exceed damage limits, hygroscopic insulation reduces freeze-thaw cycles. In low WDR areas (North), 3 cm NHL with hygroscopic insulation (PF, WFB) performs best. (Note: model overestimates liquid conductivity and rain absorption).

5.2 General conclusions

- The feedback from stakeholders indicated genuine interest and need for the solutions that were assessed in the task.
- Hydrophobation probably necessary when using NHL plaster system in high WDR conditions.
- Onset of frost damage in all tested plasters takes place between 70–100%$_{sat}$ (tested at -20°C), which is between capillary and full saturation. However, such levels were not reached even in the rather extreme conditions of the climate chamber experiment.

- Modelling results are preliminary, in case of NHL plasters it might represent the behavior of frost-damaged plaster.
- Hygroscopic insulation materials, particularly wood fibre board, demonstrated moisture-buffering effects that have the potential to reduce peak moisture contents and freeze-thaw exposure of the plaster layer, however, prolonged drying is required after the wetting periods.
- Current hygrothermal simulations should be considered conservative because the material models tend to overestimate liquid water uptake compared with experimental observations. Further calibration is therefore required before definitive performance limits can be established.

While currently TRL 5 has been reached, future work to increase it further could include:

- Adjustment of liquid transfer function to account for the water uptake and drying experiment results from thinner specimens, new comparison to outdoor and climate chamber measurements.
- Accounting for the effect of layered application of the plasters, paint, hydrophobation.
- Modelling with long-term climate files instead of repeating MRY.
- Modelling with high initial moisture content of masonry wall: might represent a moisture accumulation risk for vapour open systems.
- Modelling with intentional defects as additional moisture leaks behind the plaster for stress testing.
- Test wall on a real building incorporating larger dimensions and additional joints (e.g. window details).

Bibliography

Project deliverables

D2.1 Building envelope characteristics. https://zenodo.org/records/16317920

D2.2 Energy conservation measures inventory. https://zenodo.org/records/15364987

D3.1 HVAC concepts for heritage buildings. https://zenodo.org/records/15365094

D3.2 Comfort and IAQ in heritage townhouses. https://zenodo.org/records/16320305

D4.1 R²ES-based energy supply concepts for heritage buildings in historical neighbourhoods. https://zenodo.org/records/16321272

D5.1 Case-study selection at building and neighbourhood levels. https://zenodo.org/records/15365504

D5.2 Cultural heritage analysis and value assessment. https://zenodo.org/records/16321630

D5.3 Cultural heritage building user and owner perspectives. https://zenodo.org/records/16322452

D5.4 Baseline scenarios. https://zenodo.org/records/16322051

D5.5 Map of KPI. https://zenodo.org/records/16322322

References

Eurostat. (2022). *Energy statistics–An overview*. https://ec.europa.eu/eurostat/statistics-explained/index.php?title=Energy_statistics_-_an_overview

EVS-EN 16322 2013 Conservation of Cultural Heritage–Test methods–Determination of drying properties. (n.d.).

Feng, C., Roels, S., & Janssen, H. (2019). Towards a more representative assessment of frost damage to porous building materials. *Building and Environment*, *164*, 106343. https://doi.org/10.1016/j.buildenv.2019.106343

Grunewald, J. (1997). *Diffusiver und konvektiver Stoff- und Energietransport in kapillarporösen Baustoffen*. Technische Universität Dresden.

Häupl, P., & Xu, Y. (2001). Numerical Simulation of Freezing and Melting in Porous Materials under the Consideration of the Coupled Heat and Moisture Transport. *Journal of Thermal Envelope and Building Science*, *25*(1), 4–31. https://doi.org/10.1106/RX1L-MBE8-HUJ3-2XX3

Hukka, A., & Viitanen, H. (1999). A mathematical model of mould growth on wooden material. *Wood Science and Technology*, *33*(6), 475–485. https://doi.org/10.1007/s002260050131

Ilomets, S., Kalamees, T., & Vinha, J. (2018). Indoor hygrothermal loads for the deterministic and stochastic design of the building envelope for dwellings in cold climates. *Journal of Building Physics*, *41*(6), 547–577. https://doi.org/10.1177/1744259117718442

Imken, A. A. P., Brischke, C., Kögel, S., Krause, K. C., & Mai, C. (2020). Resistance of different wood-based materials against mould fungi: A comparison of methods. *European Journal of Wood and Wood Products*, *78*(4), 661–671. https://doi.org/10.1007/s00107-020-01554-5

Ingham, J. P. (2005). Predicting the frost resistance of building stone. *Quarterly Journal of Engineering Geology and Hydrogeology*, *38*(4), 387–399. https://doi.org/10.1144/1470-9236/04-068

Kalamees, T., & Vinha, J. (2004). Estonian Climate Analysis for Selecting Moisture Reference Years for Hygrothermal Calculations. *Journal of Building Physics*, *27*(3), 199–220. https://doi.org/10.1177/1097196304038839

Karaiskos, G., Deraemaeker, A., Aggelis, D. G., & Hemelrijck, D. V. (2015). Monitoring of concrete structures using the ultrasonic pulse velocity method. *Smart Materials and Structures*, *24*(11), 113001. https://doi.org/10.1088/0964-1726/24/11/113001

Klõšeiko, P., & Kalamees, T. (2022). Hygrothermal performance of a brick wall with interior insulation in cold climate: Vapour open vs vapour tight approach. *Journal of Building Physics*, *46*(1), 3–35. https://doi.org/10.1177/17442591211056067

Klõšeiko, P., Vilba, K., Talvik, M., Riisimäe, T. R., Lemberg, R., Põldaru, M., Võsa, K.-V., & Kalamees, T. (2026). Hygrothermal Performance of Exterior Insulation Solutions With Thick Plaster Systems Under Accelerated Weathering in Climate Chamber. *Proc. of Nordic*

Symposium on Building Physics 2026 (NSB2026). Nordic Symposium on Building Physics 2026 (NSB2026), Tampere, Finland.

Kubilay, A., Derome, D., Blocken, B., & Carmeliet, J. (2013). CFD simulation and validation of wind-driven rain on a building facade with an Eulerian multiphase model. *Building and Environment*, *61*, 69–81. https://doi.org/10.1016/j.buildenv.2012.12.005

Lemberg, R. (2026). *Evaluation of the Performance of Insulation Systems with a Thick Render Layer Based on Field Tests. Supervised by Paul Klõšeiko*. https://digikogu.taltech.ee/et/item/98cd073d-5e94-40e6-bd0b-917c6de56fd2

Liisma, E., Sepri, R., Raado, L.-M., Lill, I., Witt, E. D. Q., Sulakatko, V., & Põldaru, M. (2016). Defect analysis of renovated facade walls with etics solutions in cold climate conditions. *Proceedings of CESB16*. Central Europe towards Sustainable Building Prague 2016 (CESB16), Prague, Czechia.

Naik, T. R., Malhotra, V. M., & Popovics, J. S. (2003). The ultrasonic pulse velocity method. In *Handbook on Nondestructive Testing of Concrete, Second Edition* (pp. 8–1).

Nicolai, A., Scheffler, G. A., Grunewald, J., & Plagge, R. (2009). An efficient numerical solution method and implementation for coupled heat, moisture and salt transport: The Delphin Simulation Program. In L. Franke, G. Deckelmann, & R. Espinosa-Marzal (Eds), *Simulation of Time Dependent Degradation of Porous Materials* (pp. 85–100). Cuvillier Verlag.

Nicolai, A., & Sontag, L. (2013). Implementation of an efficient numerical solution method to simulate freezing processes in porous media. In A. Mahdavi & B. Martens (Eds), *Proceedings of 2nd Central European Symposium on Building Physics (CESBP2013)*. ÖKK-Editions.

Ojanen, T., Viitanen, H., Peuhkuri, R., Lähdesmäki, K., Vinha, J., & Salminen, K. (2010). Mold Growth Modeling of Building Structures Using Sensitivity Classes of Materials. *Proceedings of Thermal Performance of the Exterior Envelopes of Buildings XI*.

Olak, H., Kalamees, T., & Klõšeiko, P. (2026). The Statistics of Damage and Degradation of ETICS Facades. *Proc. of Nordic Symposium on Building Physics 2026 (NSB2026)*. Nordic Symposium on Building Physics 2026 (NSB2026), Tampere, Finland.

Olak, H., Talvik, M., Klõšeiko, P., Ilomets, S., & Kalamees, T. (2026, February 27). Degradation of EIFS Facades Dependent on Moisture Content of Masonry and Its Mitigation Measures. *2025 Buildings XVI International Conference*. 2025 Buildings XVI International Conference. https://doi.org/10.63044/b16ola24

Scheffler, G., & Plagge, R. (2005). Bestimmung des Trocknungsverhaltens von Baustoffen unter definierten Randbedingungen. *Bauphysik*, *27*(6), 324–330. https://doi.org/10.1002/bapi.200590088

Slapø, F., Kvande, T., Bakken, N., Haugen, M., & Lohne, J. (2017). Masonry's Resistance to Driving Rain: Mortar Water Content and Impregnation. *Buildings*, *7*(3). https://doi.org/10.3390/buildings7030070

Talvik, M., Klõšeiko, P., Kalamees, T., Liisma, E., & Ilomets, S. (2023). On site measurement and hygrothermal modelling of degraded ETICS facade with EPS and mineral wool fire breaks. *Journal of Physics: Conference Series*, *2654*(1), 012124. https://doi.org/10.1088/1742-6596/2654/1/012124

Talvik, M., Klõšeiko, P., Vilba, K., Põldaru, M., & Olak, H. (2025). Preliminary field study on hygrothermal performance of ETICS using thick lime plasters on various insulation materials for historic buildings in wet and cold climate. *Proceedings of CESBP*.

Talvik, M., Klõšeiko, P., Vilba, K., Põldaru, M., Olak, H., & Kalamees, T. (2026). Preliminary Field Study on Hygrothermal Performance of ETICS Using Thick Lime Plasters on Various Insulation Materials for Historic Buildings in Wet and Cold Climate. In B. Nagy & Z. Szalay (Eds), *Proceedings of CESBP 2025–6th Central European Symposium on Building Physics* (pp. 517–529). Springer Nature Switzerland. https://doi.org/10.1007/978-3-032-14011-1_42

Viitanen, H., Krus, M., Ojanen, T., Eitner, V., & Zirkelbach, D. (2015). Mold Risk Classification Based on Comparative Evaluation of Two Established Growth Models. *Energy Procedia*, *78*, 1425–1430. https://doi.org/10.1016/J.EGYPRO.2015.11.165

Viitanen, H., Ojanen, T., & Peuhkuri, R. (2011). Mould growth modelling to evaluate durability of materials. In V. P. de Freitas, M. H. Corvacho, & M. Lacasse (Eds), *Proceedings of the XII DBMC: 12th International Conference on Durability of Building Materials and Components*. FEUP Edições.